

# Basaltic sills emplaced in organic-rich sedimentary rocks: Consequences for organic matter maturation and Cretaceous paleo-climate

Jean H. Bédard<sup>1,†</sup>, Keith Dewing<sup>2</sup>, Stephen E. Grasby<sup>2</sup>, Peter Nabelek<sup>3</sup>, Thea Hatlen Heimdal<sup>4</sup>, Chris Yakymchuk<sup>5</sup>, Sean R. Shieh<sup>6</sup>, Justin Rumney<sup>6</sup>, Frances M. Deegan<sup>7</sup>, and Valentin R. Troll<sup>7</sup>

<sup>1</sup>Geological Survey of Canada, CGC–Québec, 491 de la Couronne, Québec, Québec G1K 9A9, Canada

<sup>2</sup>Geological Survey of Canada, 3303–33rd Street NW, Calgary, Alberta T2L 2A7, Canada

<sup>3</sup>Department of Geological Sciences, University of Missouri, Columbia, Missouri 65211, USA

<sup>4</sup>Lamont-Doherty Earth Observatory and Department of Earth and Environmental Sciences, Columbia University, Palisades, New York 10964, USA; and Centre for Earth Evolution and Dynamics, University of Oslo, Post Office Box 1028, Blindern, NO-0315 Oslo, Norway

<sup>5</sup>Department of Earth and Environmental Sciences, University of Waterloo, Waterloo, Ontario N2L 3G1, Canada

<sup>6</sup>Department of Earth Sciences, University of Western Ontario, London, Ontario N6A 5B7, Canada

<sup>7</sup>Uppsala University, Department of Earth Sciences, Natural Resources and Sustainable Development, Villavägen 16, Uppsala, Sweden

## ABSTRACT

Many continental large igneous provinces coincide with climate perturbations and mass extinctions. When basaltic plumbing systems traverse carbon-rich sedimentary rocks, large volumes of greenhouse gases may be generated. We document how intrusive sills of the Mesozoic High Arctic Large Igneous Province affected surrounding fine-grained, organic-rich siliciclastic rocks of the Sverdrup Basin in the Canadian Arctic Archipelago. Petrographic and X-ray diffraction data from samples located near sills show the presence of high-temperature metamorphic phases (diopside, andalusite, garnet, and cordierite). Raman thermometry on organic matter yields peak temperatures of 385–400 °C near sill contacts, tailing off to far-field temperatures of  $\leq 230$  °C. Samples located  $>20$  m from sills show no systematic change in vitrinite reflectance and have a  $V_{Ro}$  eq% value of  $\sim 2.5\%$ , which indicates a temperature of  $\sim 210$  °C. The finite element thermal modeling tool SUTRAHEAT was applied to the 17-m-thick Hare Sill, emplaced at 3 km depth at 1105 °C. SUTRAHEAT results show that contact-proximal rocks attain temperatures of  $>700$  °C for a brief period ( $\sim 1$  year). By 5 years, the Hare Sill is completely solidified ( $<730$  °C), and the temperature anomaly collapses rapidly thereafter as the

thermal pulse propagates outward. By 10 years, all rocks within 10 m of the Hare Sill are between 450 °C and 400 °C, rocks at 20 m from the contact attain 200 °C, yet far-field temperatures ( $>50$  m) have barely changed. When multiple sills are emplaced between 4 km and 6 km depth, all rocks between sills reach  $\sim 250$  °C after 100 years, showing that it is possible to raise regional-scale background temperatures by  $\sim 150$  °C for the observed High Arctic Large Igneous Province sill density. Vitrinite reflectance data and pyrolysis results, together with SILLi thermal modeling, indicate that much of the hydrocarbon-generating potential was eliminated by High Arctic Large Igneous Province intrusions. The SILLi model yields  $\sim 20$  tonnes/m<sup>2</sup> of organic equivalent CO<sub>2</sub> (all carbon gas is reported as CO<sub>2</sub>) from the Hare Sill alone when emplaced into Murray Harbour Formation rocks with 5.7 wt% organic carbon, and  $\sim 226$  tonnes/m<sup>2</sup> by emplacement of multiple sills throughout the 2-km-thick Blaa Mountain Group with 3 wt% organic carbon. On a basin scale, this yields a total of  $\sim 2550$  Gt CO<sub>2</sub> from the Hare Sill, with  $\sim 13,000$  Gt CO<sub>2</sub> being generated by the multiple sill scenario, similar to estimates from other large igneous provinces. Much of the Blaa Mountain Group rocks now have organic carbon contents of  $<1$  wt%, which is consistent with large volumes of carbon-species gas having been generated, likely a mixture of CO<sub>2</sub>, CH<sub>4</sub>, and other species. However, organic-rich Murray Harbour Formation rocks show no obvious reduction in organic carbon content

toward the Hare Sill intrusive contacts, which suggests that not all of the carbon was lost from the sedimentary package hosting High Arctic Large Igneous Province magmas. We suggest that some of the gas generated by contact metamorphism failed to drain out for lack of high-permeability conduits, and then back-reacted to form calcite cements and pyrobitumen during cooling.

## INTRODUCTION

Voluminous continental flood basalt provinces, a type of large igneous province (LIP), frequently coincide with notable climatic perturbations and mass extinctions (Ganino and Arndt, 2009; Svensen et al., 2009; Bond and Grasby, 2017). Heat from igneous intrusions in LIP plumbing systems creates metamorphic aureoles in the surrounding host rocks (Aarnes et al., 2010; Baker et al., 2015; Wang et al., 2010; Wang and Manga, 2015; Spacapan et al., 2018; Goodarzi et al., 2019). When carbon-rich sedimentary rocks are the hosts, the volume of volatiles released by metamorphic decarbonation reactions is potentially larger than the magmatic volatile budget. For example, Svensen et al. (2009) calculated that the Siberian Large Igneous Province released  $\sim 20,000$  Gt of magmatic-derived CO<sub>2</sub>, whereas metamorphic CO<sub>2</sub> released from heating of sedimentary rocks was estimated at  $\sim 114,000$  Gt, or  $\sim 5.7$  times greater than the magmatic CO<sub>2</sub> budget. Similarly, Ganino and Arndt (2009) calculated that contact aureoles affecting rocks of the sedimentary basin emitted up to 8.6 times the amount

Stephen E. Grasby  <https://orcid.org/0000-0002-3910-4443>

<sup>†</sup>jeanh.bedard@nrcan-mcan.gc.ca

of CO<sub>2</sub> emitted by the Emeishan Large Igneous Province intrusions in China.

The specific impact of contact metamorphic gas generation on climate will depend on the amount of gas released to the atmosphere and oceans as well as the gas species emitted, which in turn depends on the host-rock type and the temperatures attained. For example, carbon-rich sedimentary rocks would release gases like CO<sub>2</sub> and CH<sub>4</sub>, which have a warming effect in the atmosphere, whereas sulfur-rich evaporitic rocks would release SO<sub>2</sub>, causing widespread acid rain and cooling (e.g., Self et al., 2014). Moreover, as the metamorphic thermal aureoles around intrusions evolve with time, so will the breakdown reactions and the volume and compositions of the gas species emitted.

To help clarify the potential release of climate-altering gasses by LIPs, we use complementary approaches to document the impact of Mesozoic High Arctic Large Igneous Province basaltic sills on fine-grained siliciclastic host rocks of the Sverdrup Basin in the Canadian Arctic Archipelago, including some organic-rich petroleum source rocks (Fig. 1). We provide new stratigraphic thickness constraints based on studies of offshore wells and sections on land. Petrographic and X-ray diffraction data characterize mineralogical transformations caused by contact metamorphism and constrain metamorphic temperatures. We independently determined peak temperatures of sediments from vitrinite reflectance data and RAMAN thermometry on organic matter. These data are compared to results of forward modeling of heat diffusion from High Arctic Large Igneous Province sills using two independent methods. Together, these data and models imply that large volumes of greenhouse gases were produced by the High Arctic Large Igneous Province, which could have contributed to climatic perturbations (Galloway et al., 2022). Our data are also pertinent to the petroleum potential of the area and have implications for the emplacement dynamics of High Arctic Large Igneous Province magmas. Although many of our samples are depleted in organic carbon as predicted, the organic-rich Murray Harbour Formation rocks show no large-scale reduction in organic carbon content near intrusive contacts in our detailed study area, which suggests the incomplete expulsion of thermogenic gas. We suggest that some of the gas generated by contact metamorphism back-reacted with host rocks during cooling, instead of being released to the atmosphere.

## GEOLOGICAL SETTING

The Sverdrup Basin is a rift-to-sag sedimentary basin in the Canadian Arctic Archipelago (Fig. 1) deposited on deformed lower Paleozoic rocks of the Ellesmerian Orogen (Embry and Beauchamp, 2019). Sedimentation in the Sverdrup Basin was dominated in Carboniferous and Permian times by carbonate shelves around the basin margin, with mudstone and evaporite deposition in the basin center. Mesozoic sedimentation was clastic-dominated, with three large deltaic complexes that prograded over basinal and pro-deltaic mudstones. Deltaic complexes formed in the Early Triassic, Late Triassic–Early Jurassic, and Early Cretaceous. Mudstone-dominated condensed sections followed the end of the deltaic cycle in the Middle–Late Triassic, constituting the sand-bearing, basin-margin Schei Point Group and the shale-dominated, basin-center Blaa Mountain Group examined here (Fig. 1). The Schei Point and Blaa Mountain groups contain organic-rich units like the Murray Harbour Formation, which were source rocks for hydrocarbon generation (Brooks et al., 1992). Sverdrup Basin deposition continued to Late Cretaceous time, although the locus of deposition switched to the Arctic Ocean following rifting in the Early Cretaceous. Regional thermal maturity at the level of the Schei Point Group in the study area increases rapidly from the early oil window (VRo% 0.6–1.0) on Ellesmere Island to the gas window (VRo% > 1.35) on central Axel Heiberg Island (Dewing and Obermajer, 2011). Paleocene and Eocene deposition was dominated by a SW-prograding clastic wedge sourced from orogenic highlands on Ellesmere Island and Greenland. The early Cenozoic saw widespread denudation across the Arctic Islands, with 1–1.5 km of stratigraphy being removed (Dewing and Obermajer, 2011).

The Cretaceous to Paleogene High Arctic Large Igneous Province is manifested as dikes, sills, lava flows, and volcanogenic sediments, and was possibly related to the arrival of a mantle plume beneath the Alpha Ridge (Embry and Osadetz, 1988; Maher, 2001; Buchan and Ernst, 2006; Tegner et al., 2011; Døssing et al., 2013; Estrada, 2015; Bédard et al., 2021a, 2021b; Naber et al., 2021). Continental tholeiitic magmatism started at ca. 130 Ma, whereas alkaline magmatism started at ca. 94 Ma in Canada, and slightly later (at ca. 85 Ma) in Greenland (Estrada and Henjes-Kunst, 2004, 2013; Tegner et al., 2011; Bédard et al., 2021b). Geochronological data imply two main phases of tholeiitic magmatism in the Sverdrup Basin, one at ca. 122 Ma and another at ca. 95 Ma (Kingsbury et al., 2018; Dockman et al., 2018). High Arctic Large Igneous Province sills extend over 1000 km, from the western Sverdrup Basin to NE Ellesmere Island (Saumur et al., 2016), and are most commonly hosted by Triassic and Jurassic mudstone, siltstone, and sandstone. Sills do occur in Carbonif-

erous–Permian strata (Fig. 1), but few drill holes penetrate the (poorly exposed) upper Paleozoic section, making the extent of sill emplacement there very uncertain.

## SAMPLE BASE AND SECTIONS

For this study, samples of sedimentary host rocks and High Arctic Large Igneous Province intrusions were collected from three sites on Axel Heiberg Island (Schei Point, Mokka Fiord, and Northern Geodetic Hills) and three sites on Ellesmere Island (Blue Mountains and North and South Hare Fiord; Fig. 1). Outcrop samples are complemented by data derived from hydrocarbon exploration well core and cuttings (Dewing and Embry, 2007). There are 28 petroleum boreholes in the Sverdrup Basin penetrating the Heiberg Formation or Schei Point/Blaa Mountain groups that intersected a total of 244 sills. The wells were drilled between 1971 and 1986 and were analyzed post-drilling with a limited suite of downhole logs typical of that era: gamma-ray, sonic, density, and caliper. Sample descriptions are in well history reports filed with the Canadian National Energy Board. Formation tops and collar location data are in Dewing and Embry (2007).

The highest concentrations of sills in exploration boreholes are on Axel Heiberg, Amund Ringnes, and Ellef Ringnes islands. The interval between the highest sill and lowest sill in a well segment containing abundant sills can consist of ~20% igneous rock (Fig. 2). Sills in wells vary between 0.60 m and 143 m thickness, with a median of ~10 m, while the interval between sills is between 27 cm and 600 m, with a median of 15.4 m (Fig. 2; Table 1). Sills are only slightly more common in mudstone + siltstone than in sandstone, with 16.7% of mudstone + siltstone intervals in the intruded intervals occupied by sills, as compared to 13.5% of the sandstone intervals being occupied by sills. Present depth of sills ranges from 100 m to 4900 m, with an average of 1900 m (Fig. 2). Although not constrained by radiometric age dating, the sills in wells are considered to be associated with the High Arctic Large Igneous Province, as this is the only known widespread Phanerozoic igneous event in Arctic Canada (Ernst, 2014).

High Arctic Large Igneous Province sills are composed of sparsely phryic tholeiitic diabase (<10% olivine + plagioclase + clinopyroxene phenocrysts and antecrysts), with less common thicker sills (≥30 m) having more gabbroic textures (Bédard et al., 2021a). Most sedimentary rocks sampled belong to the Triassic Blaa Mountain Group (Fig. 1B, Anisian to Norian; Dewing and Embry, 2007), which is dominated by siltstone and mudstone with subordinate

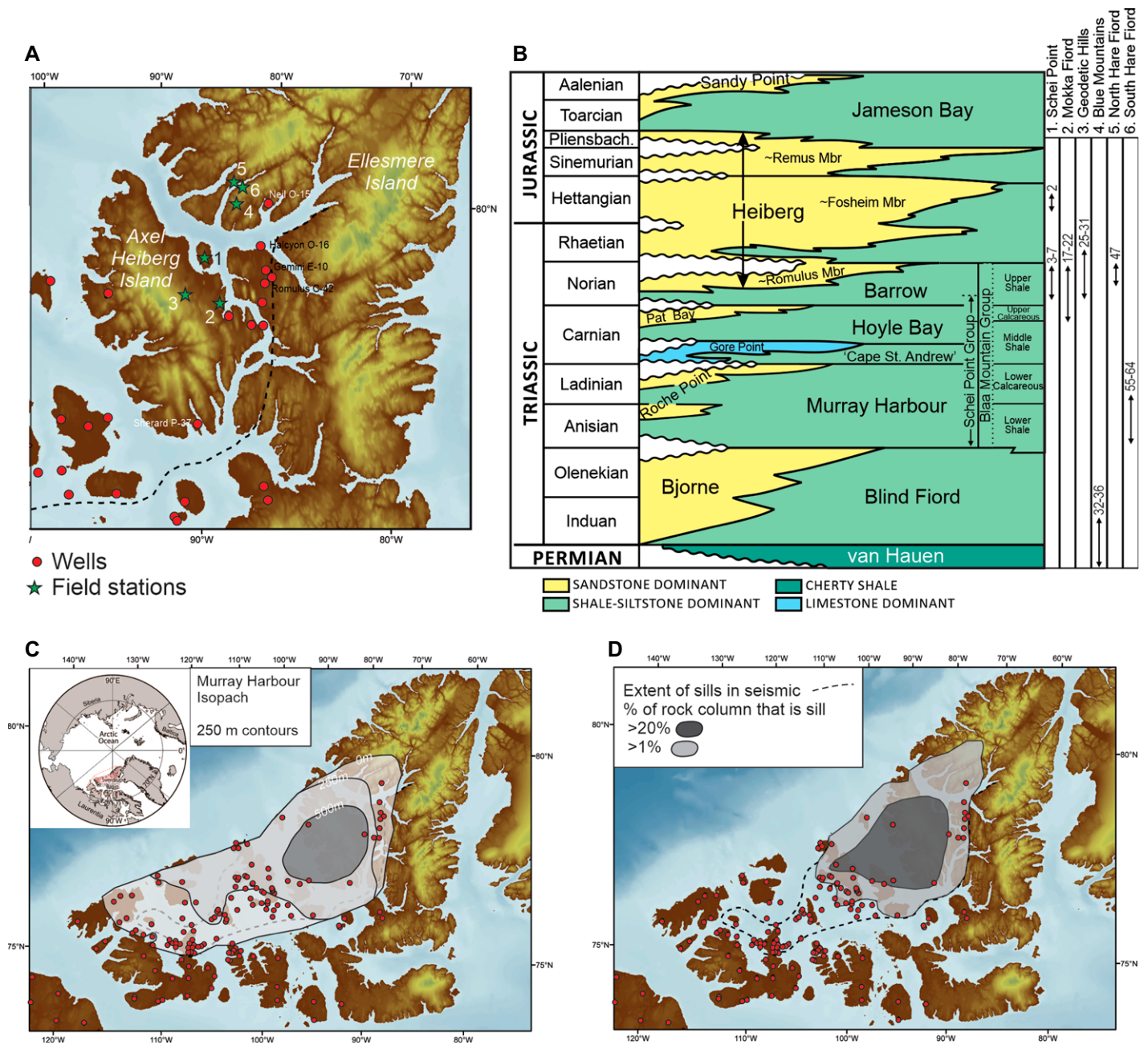


**Figure 1.** (A) Locations of sections studied and wells. Sections: 1—Schei Point; 2—Mokka Fiord; 3—Geodetic Hills; 4—Blue Mountains; 5—North Hare Fiord; 6—South Hare Fiord (Hare Sill). Grey dashed line shows limit of sill emplacement. See inset in panel C for the locations of Axel Heiberg Island and Ellesmere Island. (B) Permian to Jurassic stratigraphy of the Sverdrup Basin after Tozer (1961), Embry (1984), and Embry and Beauchamp (2019). The Schei Point Group includes basin-margin formations (Murray Harbour to lower Barrow, Roche Point, Gore Point, and Pat Bay formations). The Blaa Mountain Group includes basin-center correlatives of the Schei Point Group. Tozer (1961) divided the Blaa Mountain Group into shale and calcareous intervals. The stratigraphic levels sampled at each site are shown at right (the 15BEB- prefix in sample names is omitted here). (C) Isopach map of Schei Point Group based on thicknesses in Dewing and Embry (2007). Locations of wells are also shown. The location of the study area is shown in the inset polar projection map (red dashed line). (D) Dashed line shows extent of sills in seismic data (Saumur et al., 2016), and shaded polygons show percentage of the rock column that is composed of sills.

fine-grained sandstone. The Anisian/Ladinian Murray Harbour Formation of the Schei Point Group and its correlatives in the Blaa Mountain Group are especially rich in organic matter and

are an important source rock for hydrocarbons in the Sverdrup Basin (Brooks et al., 1992; Gentzis et al., 1996; Mukhopadhyay et al., 1997; Kondla et al., 2015; Grasby et al., 2016), which is why

we focus on this unit. Dark mudstone samples from the upper Permian van Hauen Formation (Blue Mountain Section), siltstones from the Lower Triassic Blind Fiord Formation, and sand-

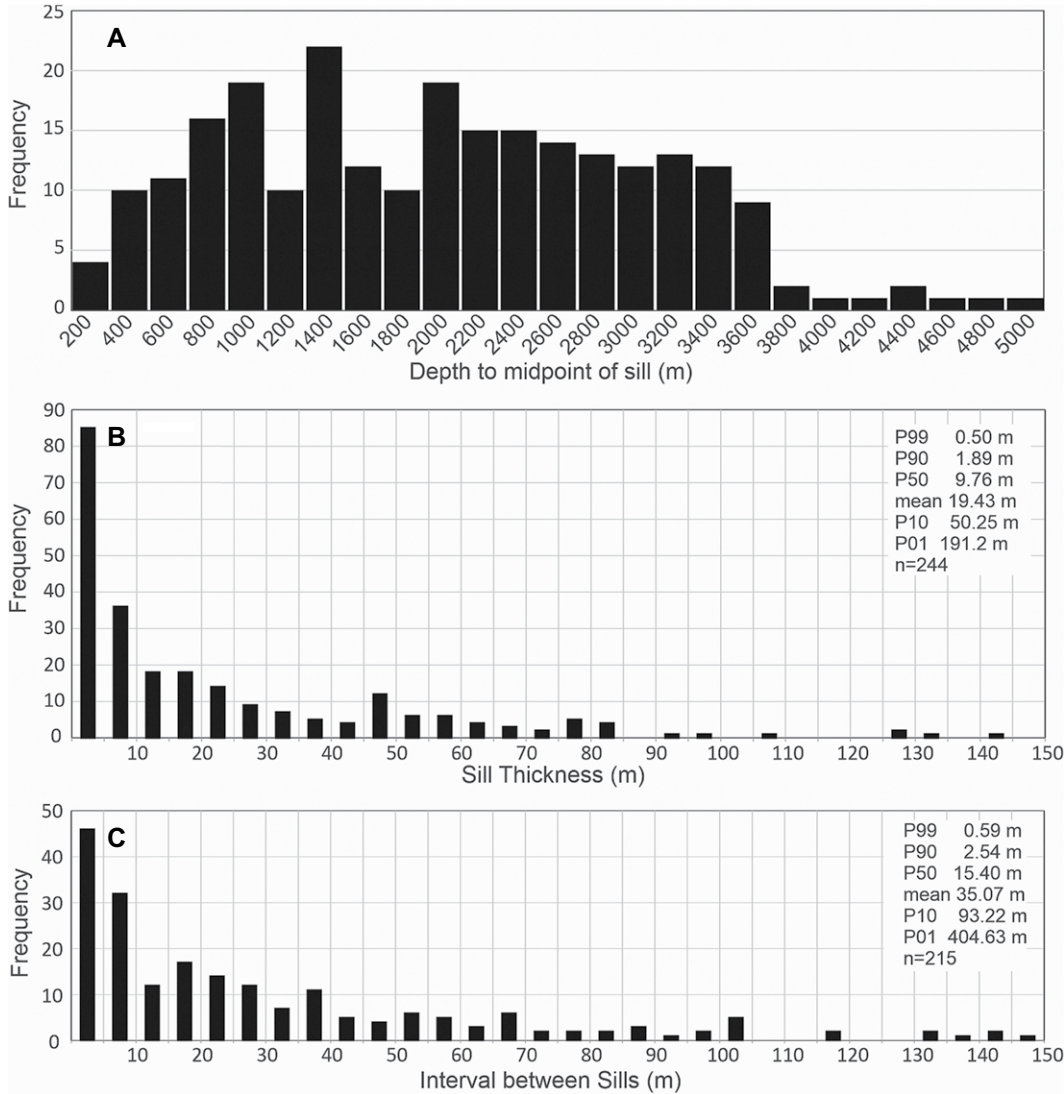


TABLE 1. DISTRIBUTION OF SILL THICKNESSES AND INTERVALS BETWEEN SILLS FROM DRILLHOLE DATA

Stratigraphic unit	Intersected thickness (m)	Sill thickness (m)	Lithology	n =	Average thickness (m)	Percentage	TOC P90	TOC P50	TOC P10	Emplacement depth (m)
Deer Bay FM	2022.2	375.2	sh	10	35.7	18.6	0.73	1.79	3.27	0–1000
Awingak FM	132.6	3.3	ss	1	3.3	2.5	0.54	2.51	5.66	500–1000
Ringnes FM	1221.2	452.0	sh	14	32.3	37.0	1.45	3.49	6.30	500–1600
McConnell Island FM	1610.6	382.5	sh	18	21.3	23.7	0.72	2.26	4.55	1200–2000
Sandy Point FM	384.0	0.0	ss	0	0	0.0	0.29	1.20	2.63	650–1000
Jameson Bay FM	1843.6	231.6	sh	15	15.4	12.6	0.39	1.17	2.32	900–2400
Heiberg FM	7564.5	1038.1	ss	47	22.1	13.7	0.19	1.69	4.27	1000–3000
Grosvenor Island FM	257.7	64.4	sh	2	32.2	25.0	0.38	0.89	1.60	
Barrow FM	5068.3	735.5	sh	46	16.4	14.5	0.36	0.94	1.75	1700–3300
Pat Bay FM	232.2	81.1	ss	2	40.5	34.9	0.22	0.80	1.67	2700–3500
Hoyle FM	3926.8	537.7	sh	31	17.3	13.7	0.36	2.15	5.13	2800–3500
Gore Point MBR	104.3	0.0	lst	2	2.8	0.0				
Roche Point FM	391.1	14.4	ss	1	8.8	3.7	0.14	1.16	2.92	
Murray Harbour FM	1292.9	260.0	sh	11	23.6	20.1	0.28	1.11	2.42	
Bjorne FM	5202.6	653.1	ss	22	29.7	12.6	0.05	0.36	0.88	
Blind Fiord FM	4288.9	534.0	sh	19	26.9	12.5	0.09	0.40	0.88	
Degerbols FM	229.2	140.2	ss	2	70.1	61.2				
Assistance FM	352.0	29.6	ss	1	29.6	8.4	0.14	0.40	0.77	
Van Hauen FM	404.2	116.5	sh	1	116.5	28.8	0.09	0.57	1.36	
Hare Fiord FM	873.2	109.5	sh	2	54.7	12.5	0.36	0.95	1.79	
Sandstone	14,488.2	1959.8		76		13.5				
Shale	22,809.6	3798.9		169		16.7				

Note: TOC—total organic content; P50 = median value (P10 and P90 signify 10% and 90% of data are above this value, respectively); FM—formation; MBR—member; sh—shale; ss—sandstone; lst—limestone.

stones from the Lower Jurassic Heiberg Formation were also examined, making our results more generally applicable.

## SAMPLE SECTIONS

At most stations, we collected sill-proximal (<1 m from contact) and more distal (3–5 m) sample pairs. We collected longer sample profiles from outcrop at two sites (Blue Mountain and South Hare Fiord), measuring the distance from the intrusive contact. The distances appended to sample numbers here are the distance to the nearest intrusive contact in meters. Detailed location maps, field descriptions, and thin section descriptions of samples are in File S1 in the Supplemental Material<sup>1</sup>.

### Schei Point

The Schei Point section (stations 15BEB-2 to 15BEB-7; Fig. S1) has steeply dipping diabasic intrusions up to 20 m thick that trend NW. Most intrusions are concordant with bedding, are typically 2–5 m wide, and are spaced ~50–100 m apart. Intrusions at station 15BEB-2 are hosted by tan, fine-grained, quartz-rich sandstone and gray siltstone of the Lower Jurassic Heiberg Formation (Fig. 1), whereas other stations (15BEB-3 to 15BEB-7) are siltstones and silty mudstone from the uppermost part of the Middle to Upper Triassic Blaa Mountain Group. Fine-grained siliciclastics located >2 m from sills are dark gray, contain diagenetic pyrite, and may have an oily appearance, whereas samples located <2 m from sills are paler (Fig. 3F), and many contain metamorphic porphyroblast pseudomorphs.

### Mokka Fiord

Mokka Fiord's (stations 15BEB-17 to 15BEB-22; Fig. S2) dikes and sill-like intrusions are widely spaced, trend NW, and dip ~40°E. Thicker intrusions are ~30 m thick and display gabbroic textures. Gabbroic sills are cut by thinner N-NE-trending tholeiitic dikes. Host rocks of the upper Blaa Mountain Group are gray siltstone, with subordinate laminated sandstone and dark silty mudstones. Intrusions have bleached haloes that are 2–3 m wide. Metamorphic porphyroblast pseudomorphs were observed up to 20 m from intrusive contacts (Fig. 3G).

<sup>1</sup>Supplemental Material. Includes field and thin section descriptions, XRD results, complete whole-rock data and coordinates, organic matter reflectance and Rock Eval data, and input parameters for the SILLi modeling. Please visit <https://doi.org/10.1130/GSAB.S.23717655> to access the supplemental material, and contact [editing@geosociety.org](mailto:editing@geosociety.org) with any questions.

### Northern Geodetic Hills

Sills of the Northern Geodetic Hills (stations 15BEB-25 to 15BEB-31; Fig. S3) are thicker (10–50 m) and more closely spaced than in other sections, constituting ~30% of outcrop. This major N-S-trending sill swarm extends >100 km along-strike and constitutes a major part of the Schei Sills discussed in Saumur et al. (2022). Sill contacts trend NW and dip ~40°E, but contacts are offset by E-W-trending syn-magmatic normal faults containing parasitic diabasic intrusions (fig. 2 in Bédard et al., 2016). Stations 15BEB-25 to 15BEB-29 are in the Heiberg Formation, which is mostly composed of gray siltstone and quartz-rich sandstone. Contact-proximal sedimentary rocks are typically bleached, and a pyrite-rich metasedimentary septum (<1 m wide) between two sills was sampled. Intrusions at stations 15BEB-30 and 15BEB-31 are hosted by dark, silty mudstones of the upper Blaa Mountain Group.

### Blue Mountains

Sills in the Blue Mountains section (stations 15BEB-32 to 15BEB-36; Fig. S4) are 2–30 m thick and constitute ~10%–15% of the section. There are rare NW-trending tholeiitic dikes (station 15BEB-40). An ~85 m measured section beneath a 20- to 30-m-thick sill (station 15BEB-32) was sampled in dark pyritic mudstones of the upper Permian van Hauen Formation. Stations 15BEB-33 to 15BEB-35 are located in the Lower Triassic Blind Fiord Formation, which is composed here of black to gray silty mudstones and siltstone. Stations 15BEB-36 to 15BEB-40 are sandstones and gray siltstones from the upper Blaa Mountain Group.

### North Hare Fiord

In the North Hare Fiord section sample 15BEB-47 (Fig. S5), a single sill-proximal pale siltstone sample was collected from the Norian Barrow Formation (equivalent to upper Blaa Mountain Group).

### South Hare Fiord

On the southern shore of Hare Fiord (samples 15BEB-55 to 15BEB-64; Fig. S5), there are several widely spaced, E-W-trending, shallowly south-dipping sills and oblique dikes (Figs. 3A and 3B). The Hare Sill is hosted by dark mudstone and siltstone of the Murray Harbour Formation (equivalent to the lower shale, Blaa Mountain Group, Anisian/Ladinian; Embry and Beauchamp, 2019). The dark siliciclastic rocks are rich in diagenetic pyrite (Fig. 4D) and organic

material (Figs. 4F and 4G), with subordinate 5- to 30-cm-thick interbeds of dolostone and phosphoric rocks (Figs. 3B and 4H). Visible contact-metamorphic effects are limited, and there are well-preserved macrofossils within meters of the Hare Sill lower contact (Fig. 3C). A 55 m section (station 15BEB-60, Fig. 3A) through the host rocks beneath the Hare Sill was measured and sampled, together with shorter contact-proximal sections above (stations 15BEB-57 and 15BEB-59) and below intrusive contacts (stations 15BEB-55 and 15BEB-58). Two distal samples (samples 15BEB-63 and 15BEB-64) were collected ~60 m beneath the eastward termination of the Hare Sill, and ~50 m above a subjacent gabbroic sill.

The Hare Sill pinches and swells (Fig. 3A) and ends to the east of station 15BEB-60 (Fig. 3B). We collected a detailed sample section through the sill at station 15BEB-56, where it is 17 m thick. The sill's upper contact is generally parallel to bedding, but it can shift abruptly up- or down-section by several meters along-strike. The contact is locally brecciated, and centimeter- to meter-scale magmatic apophyses (dikelets) are common both above and below the main sill. The lower contact of the Hare Sill is mostly parallel to bedding, and there are prominent sulfide coatings on joint surfaces (Fig. 3E). Pale, centimeter-sized leucocratic hydrothermal veins occur in the hornfelsed mudstone immediately beneath the Hare Sill's lower contact. Intrusive contacts are locally decorated by beads of magmatic sulfides (Deegan et al., 2022). Secondary (metasomatic) pyrite is observed throughout the sill, but is especially prominent near the lower contact, where replacive pyrite nodules of up to 1 cm in size are observed (Deegan et al., 2018).

## ANALYTICAL METHODS

### Mineralogy

X-ray diffraction (XRD) analyses were carried out at the University of Waterloo in Ontario, Canada. Samples were crushed in a stainless-steel mortar and pestle until they passed 2 mm mesh sieves and were then pulverized in a Retsch PM 200 Planetary Ball Mill using stainless-steel containers until >95% of the powder passed a 63- $\mu$ m mesh. Milling containers were cleaned with quartz sand between samples. X-ray diffraction patterns were collected using a PANalytical Empyran Series 2 X-ray diffractometer at 40 kV and 45 mA using Co K $\alpha$  radiation from 3°2 $\theta$  to 70°2 $\theta$  in steps of 0.01°2 $\theta$ . Six samples (15BEB-32B, 15BEB-32D, 15BEB-32G, 15BEB-59A, 15BEB-59D, and 15BEB-60H) were analyzed for 12 h to develop detailed spectra patterns

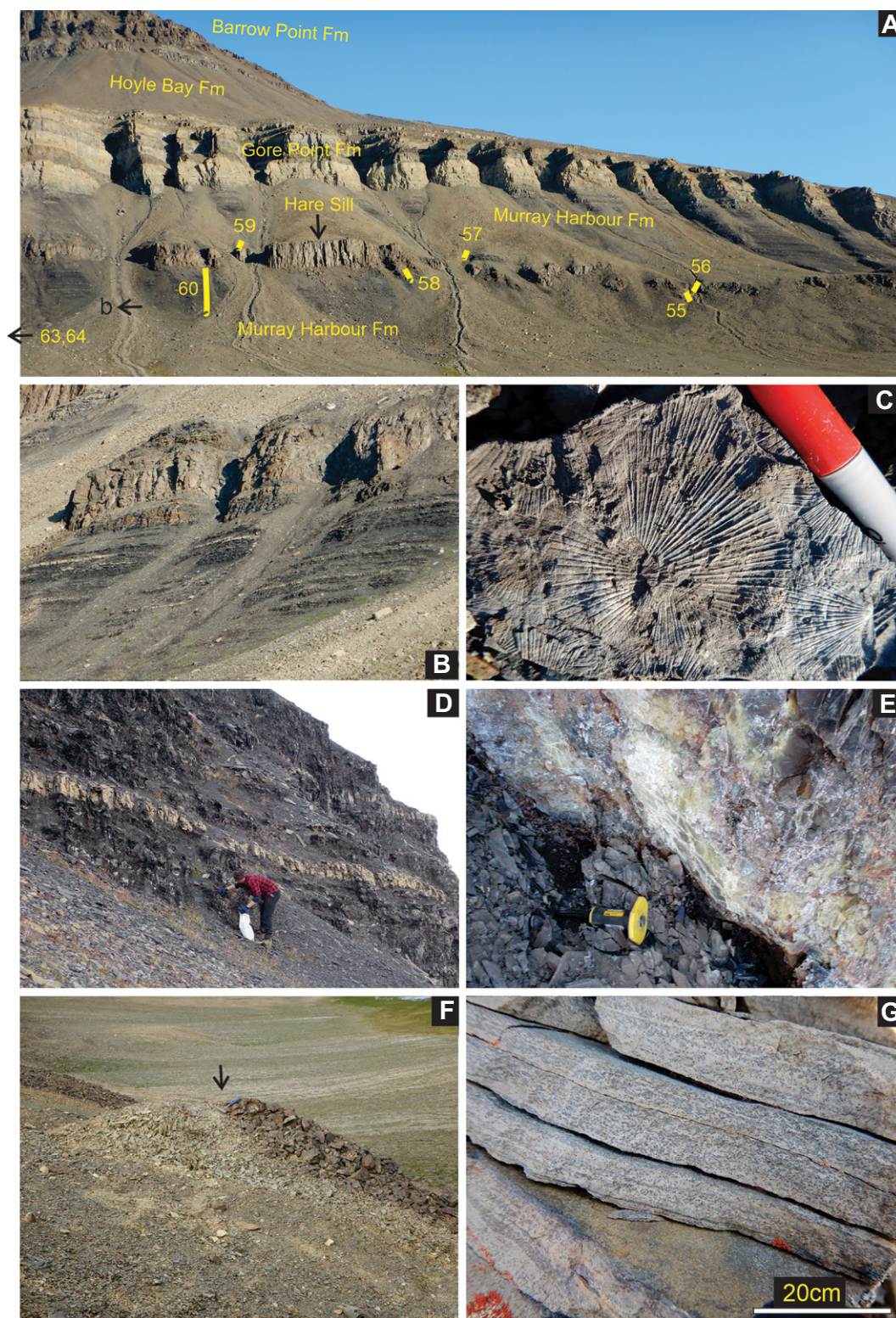
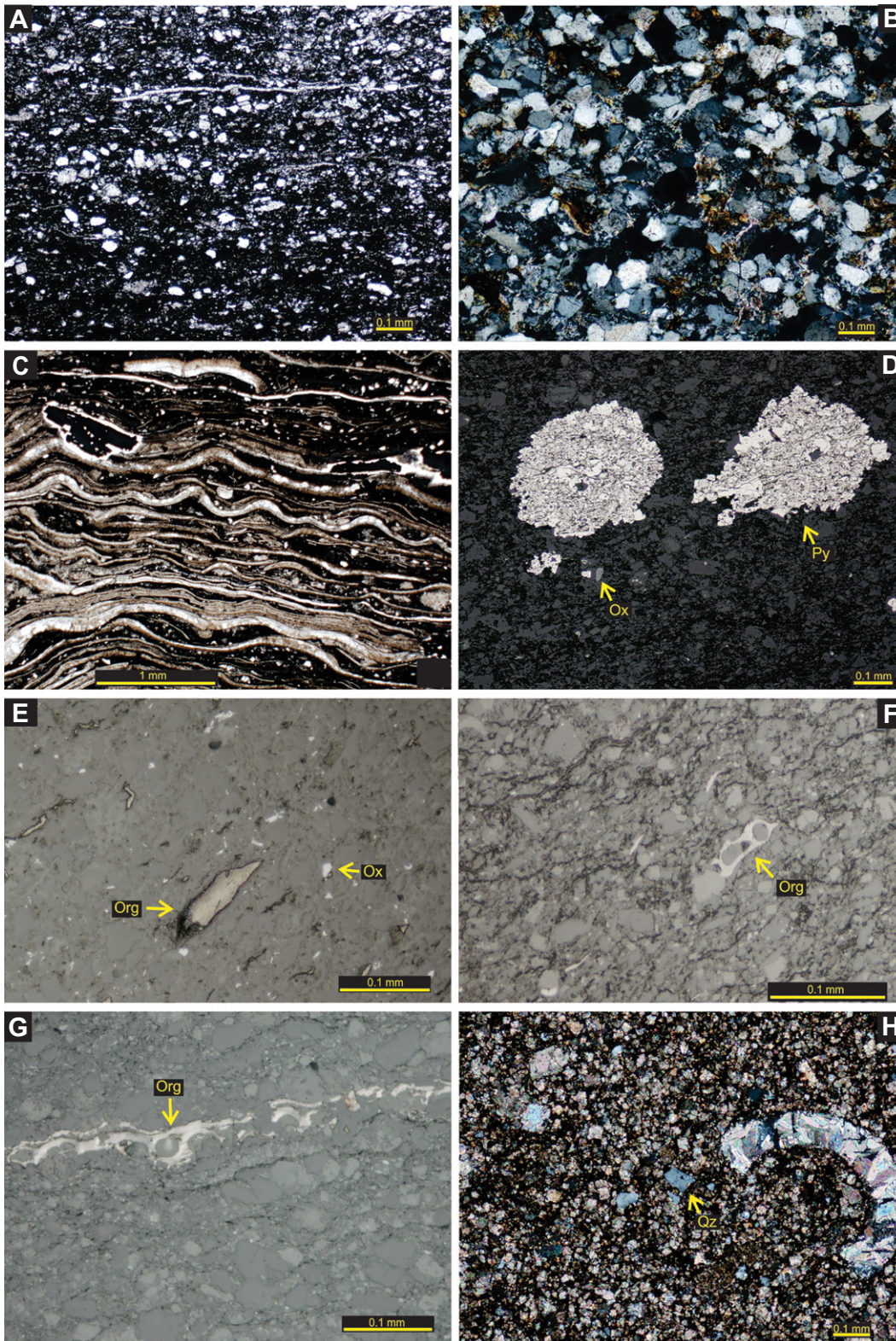


Figure 3. (A) South Hare Fiord site (Fig. 1B; Fig. S5 [see text footnote 1]), view to the south. The numbered yellow bars are the sample sections through the Hare Sill that host Murray Harbour Formation siliciclastics. Section 15BEB-60 is ~55 m thick, while the sill at section 15BEB-56 is 17 m thick. Note the lateral variations of the Hare Sill's thickness and position in the mudstone. Capping Formations are Gore Point carbonates, Hoyle Bay mudstones, and Barrow Point sandstones. The black arrow marked b is the viewpoint of Figure 3B. (B) View to the east of Murray Harbour Formation. Paler layers are carbonates embedded in darker mudstone/siltstone. The Hare Sill forms the capping buttress here. Note the presence of thin sill apophyses within the sedimentary rocks just below the main part of the sill. (C) *Minotis* pelecypod fossil on bedding plane in Murray Harbour Formation mudstone. Pen is 16 mm wide. (D) Close-up view of mudstone/siltstone (dark) and carbonate (light) layers from base of section 60, Murray Harbour Formation. (E) Lower contact of Hare Sill. Note the prominent sulfur staining, which suggests that S-rich fluids/gases from the underlying sedimentary rocks veined the overlying sill. Chisel is shown for scale. (F) Heiberg Formation siltstone beneath inclined sill remnant (reddish mound with hammer; see black arrow). Note how formerly dark, organic C-rich siliciclastics are bleached for ~2 m below the sill (Schei Point section). (G) Contact-metamorphosed section of Blaa Mountain Group adjoining dike, station 15BEB-17 (Mokka Fiord section). Note prominent porphyroblasts. Scale bar is ~20 cm.

(e.g., fig. 1 in File S2). The remaining 34 samples were analyzed for 2 h (e.g., fig. 2 in File S2). The identification of crystalline phases in

the XRD scans was performed using PANalytical HighScore Plus (version 3.0.5) with a database from the vendor, which includes the

International Centre for Diffraction Data PDF 4 + database and the Crystallography Open Database.



**Figure 4.** Photomicrographs of representative sedimentary rocks samples. (A) Representative mudstone from Murray Harbour Formation, sample 15BEB-58D, viewed in transmitted light. Clasts (~15%) are quartz > plagioclase > altered mafics > Fe-Ti oxides. Note bedding-parallel pale fibers (muscovite?) and dark platy grains of uncertain origin. (B) Representative fine-grained sandstone from Savik Formation (Schei Point section), crossed Nicols, sample 15BEB-2B. (C) Possible algal structures in mudstone from Murray Harbour Formation, viewed in transmitted light, sample 15BEB-60G2. (D) Probable diagenetic pyrite (Py) and detrital Fe-Ti oxides (Ox) from Murray Harbour silty mudstone, sample 15BEB-59F, viewed in reflected light. (E) Irregular blebs of reflective organic matter (Org) in silty mudstone, sample 15BEB-3 from the Heiberg Formation (Schei Point section), viewed in reflected light. (F) Blebs of organic matter in Murray Harbour silty mudstone, sample 15BEB-55D. Note how organic matter surrounds small rounded clasts. Viewed in reflected light. (G) Veinlet of organic matter in Murray Harbour Formation silty mudstone, sample 15BEB-57B, viewed in reflected light. (H) Fine-grained calci-siltite packstone, sample 15BEB-60D1 from Murray Harbour Formation. Crossed Nicols. Note the subordinate angular quartz clasts (Qz) and the fossil fragment.

From the XRD analyses, the best-fit mineral identifications and their weight fractions (calculated by HighScore Plus) are summarized in File S2. Complete XRD output for each sample is

in File S3, which includes the main peaks identified, the  $2\theta$  values, semiquantitative mineral weight proportions, and the operating conditions. Note that the weight fractions were not normal-

ized to account for the non-crystalline carbonaceous material that makes up a large proportion of some samples. There are some samples where the predicted minerals from the XRD profiles are

TABLE 2. MINERAL CHEMICAL ANALYSES

Sample	15BEB-55B		15BEB-58C1							
	Mineral	Chromite	Datolite		Prehnite		Apophyllite		Calcite	
n	2		5		2		4		3	
SiO <sub>2</sub>	0.379	SiO <sub>2</sub>	36.67	SiO <sub>2</sub>	42.35	SiO <sub>2</sub>	51.0	MgCO <sub>3</sub>	0.025	
TiO <sub>2</sub>	0.131	TiO <sub>2</sub>	<dl	TiO <sub>2</sub>	<dl	TiO <sub>2</sub>	0.014	CaCO <sub>3</sub>	98.7	
Al <sub>2</sub> O <sub>3</sub>	12.19	Al <sub>2</sub> O <sub>3</sub>	0.016	Al <sub>2</sub> O <sub>3</sub>	19.08	Al <sub>2</sub> O <sub>3</sub>	0.016	MnCO <sub>3</sub>	0.028	
Cr <sub>2</sub> O <sub>3</sub>	50.52	Cr <sub>2</sub> O <sub>3</sub>	0.011	Cr <sub>2</sub> O <sub>3</sub>	<dl	Cr <sub>2</sub> O <sub>3</sub>	0.005	FeCO <sub>3</sub>	0.058	
FeO	27.38	FeO	0.012	Fe <sub>2</sub> O <sub>3</sub>	6.8	FeO	0.0038	SrCO <sub>3</sub>	<dl	
NiO	<dl	MgO	0.0098	MgO	0.011	MgO	0.009	Na <sub>2</sub> CO <sub>3</sub>	0.017	
MgO	1.059	CaO	35.26	CaO	26.75	CaO	24.83	K <sub>2</sub> CO <sub>3</sub>	0.0057	
CaO	0.489	MnO	0.013	MnO	0.018	MnO	0.01			
MnO	<dl	Na <sub>2</sub> O	0.012	Na <sub>2</sub> O	0.046	Na <sub>2</sub> O	0.045			
Na <sub>2</sub> O	0.068	K <sub>2</sub> O	0.0012	K <sub>2</sub> O	0.0035	K <sub>2</sub> O	3.33			
CoO	0.096									
ZnO	3.84									
Total	96.16	Total	72.0	Total	95.07	Total	79.26	Total	98.87	
Cations	24		1		14		13		2	
Si	0.111	Si	0.4919	Si	6.004	Si	8.0855	MgCO <sub>3</sub>	0.00067	
Ti	0.029	Al	0.00026	Al	3.189	Ti	0.0016	CaCO <sub>3</sub>	1.997	
Al	4.192	Cr	0.00012	Mg	0.0023	Al	0.003	MnCO <sub>3</sub>	0.00033	
Cr	11.649	Mg	0.0002	Ca	4.065	Cr	0.0007	FeCO <sub>3</sub>	0.001	
Fe <sup>2+</sup>	6.679	Ca	0.507	Mn	0.0022	Mg	0.002	Na <sub>2</sub> CO <sub>3</sub>	0.00033	
Mg	0.46	Mn	0.00015	Fe <sup>3+</sup>	0.7245	Ca	4.2186			
Ca	0.03	Fe	0.00014	Na	0.013	Mn	0.0014			
Co	0.022	Na	0.00031	K	0.0006	Fe	0.0005			
Zn	0.828	K	0.00002			Na	0.0139			
Na	0.038					K	0.6728			
Cr/Cr + Al	73.54	B	0.5			F	1			
		OH	0.5			OH	8			
		Analysis recalculated to 100 wt%			Analysis recalculated to 100 wt%					
		SiO <sub>2</sub>	40.79			SiO <sub>2</sub>	52.92			
		Al <sub>2</sub> O <sub>3</sub>	0.018			TiO <sub>2</sub>	0.014			
		Cr <sub>2</sub> O <sub>3</sub>	0.012			Al <sub>2</sub> O <sub>3</sub>	0.017			
		MgO	0.011			Cr <sub>2</sub> O <sub>3</sub>	0.005			
		CaO	39.22			MgO	0.009			
		MnO	0.014			CaO	25.76			
		FeO	0.014			MnO	0.011			
		Na <sub>2</sub> O	0.013			FeO	0.004			
		K <sub>2</sub> O	0.0013			Na <sub>2</sub> O	0.047			
		B	7.47			K <sub>2</sub> O	3.451			
		H <sub>2</sub> O	12.43			F	2.069			
						H <sub>2</sub> O	15.7			

Note: Average mineral analyses. 15BEB-55B is a mudstone/siltstone. 15BEB-58C1 is a centimeter-sized vein hosted by hornfelsed mudrocks immediately below Hare Sill. n—number of spot analyses in average; <dl—below detection limit; Cations—number of cations in mineral structure. For datolite [CaBSiO<sub>4</sub>(OH)] and apophyllite [(K,Na)Ca<sub>4</sub>(Si<sub>4</sub>O<sub>10</sub>)2F·8(H<sub>2</sub>O)], neither B nor F were determined, but strong B and F peaks were detected in qualitative scans. The formula was calculated assuming the ideal mineral stoichiometry, and the analyses were recalculated to 100 wt% on this basis.

different from the observed minerals in thin section. These are discussed in detail below. The focus was on silicate and carbonate minerals, as the relatively low proportion of sulphide minerals in most samples precluded a more detailed breakdown of sulphide mineral species.

Minerals in selected samples were analyzed with a Cameca SX 100 electron probe at Laval University, Québec, Canada (Table 2). This instrument has five wavelength-dispersive spectrometers. Minerals were analyzed using a focused beam (1 µm in diameter) according to the analytical conditions described in Hayes et al. (2015). Mineral formulae were reduced or reconstructed assuming stoichiometry.

#### Whole-Rock Major and Trace Element Geochemistry

Weathered rinds were removed with a diamond saw, and saw marks were removed with a grinding wheel. Samples were crushed in a tungsten carbide shatterbox and analyzed at Actlabs, Ancaster, Ontario, using their research-

grade packages Code 4LITHORES. Lithium metaborate/tetraborate fusion was followed by analysis by fusion inductively coupled plasma-emission spectroscopy (ICP-ES, for major and minor elements) and fusion inductively coupled plasma-mass spectrometry (ICP-MS, trace elements) on a PerkinElmer SCIEX ELAN 6000, 6100, or 9000 ICP-MS. The following detection limits given by Actlabs were used. For rare earth elements (REEs), 0.05 ppm for La, Ce, and Nd; 0.01 ppm for Pr, Sm, Gd, Tb, Dy, Ho, Er, and Yb; 0.002 ppm for Lu; and 0.005 ppm for Eu and Tm. For other trace elements, detection limits were 5 ppm for Pb; 1 ppm for Rb; 0.2 ppm for Nb; 0.1 ppm for Cs and Hf; 0.01 ppm for Ta and U; and 0.05 ppm for Th and Tl. We compared duplicate analyses generated at the Institut National de la Recherche Scientifique Eau, Terre et Environnement Laboratory in Québec City (for methods and error estimates, see Leclerc et al., 2011) and found them to be essentially identical for the High Arctic Large Igneous Province compositional range. Siderophile ele-

ments were analyzed at LabMaTer (Chicoutimi, Canada); see Savard et al. (2010) for methods. Representative data are in Table 3. Complete data are in File S4.

#### Carbon Isotopes

The carbon isotope values of organic carbon were determined at the J. Veizer Laboratory at the University of Ottawa, Ontario. Calibrated internal standards were prepared with every batch of samples for normalization of the data. After acid leaching and rinsing to remove carbonate minerals, solids were weighed in tin capsules, and the isotopic composition of organic carbon (and nitrogen) was determined by analyzing CO<sub>2</sub> (and N<sub>2</sub>) produced by combustion on an Elementar vario EL cube elemental analyzer followed by "trap and purge" separation and online analysis by continuous flow with a DELTAPlus Advantage isotope ratio MS coupled with a ConFlo III interface. The routine precision of the analyses is 0.20‰. Data and duplicate runs are provided in File S4.



Contact metamorphism of black shale

TABLE 3. REPRESENTATIVE AND AVERAGE WHOLE-ROCK ANALYSES

15BEB-	4B	32G	58B	57C	57F	60E	55H	Hare Sill
Rock type	m/s	m	mh	m	p/s	c/s	c	Diabase
Area	SP	BM	SHF	SHF	SHF	SHF	SHF	SHF
m from contact	1	-85	0.05	3	9	-38.5	-20	
<b>wt%</b>								
SiO <sub>2</sub>	56.24	81.66	53.91	49.89	46.78	29.44	6.58	50.12
TiO <sub>2</sub>	0.801	0.388	0.549	0.481	0.432	0.281	0.099	2.59
Al <sub>2</sub> O <sub>3</sub>	18.14	6.00	11.21	10.78	8.43	5.32	1.97	13.30
FeO <sub>t</sub>	9.04	2.82	3.26	2.52	2.09	4.26	3.43	13.60
MnO	0.14	0.075	0.065	0.04	0.025	0.086	0.128	0.23
MgO	2.35	1.21	2.11	1.43	2.25	7.24	11.55	5.43
CaO	0.87	0.66	17.51	20.65	17.13	22.84	35.29	9.73
Na <sub>2</sub> O	1.73	0.34	0.14	0.11	1.34	0.22	0.02	2.39
K <sub>2</sub> O	2.57	0.93	0.11	0.06	2.2	0.89	0.05	0.53
P <sub>2</sub> O <sub>5</sub>	0.29	0.09	0.04	0.03	4.99	0.03	0.43	0.25
LOI	5.51	4.39	10.56	12.39	13.2	29.23	38.39	0.46
Total	98.69	98.9	99.83	98.66	99.09	100.3	98.33	100.09
C	0.66	1.3	7.92	5.42	4.6	9.28	11.2	0.0005
S	0.032	0.368	0.151	0.349	0.482		0.246	0.061
N	0.119	0.044	0.010	0.058	0.141		0.001	
H	0.609	<dl	0.405	0.383	0.382		0.245	0.077
<b>ppm</b>								
Cs	7.1	2.9	<0.1	0.1	1.5	2.6	0.1	1.153
Rb	131	44	3	1	79	41	3	175
Ba	339	826	27	53	1991	411	996	155.7
Th	13.6	4.81	7.23	6.14	5.55	3.49	1.33	1.925S
U	2.54	3.97	10.8	9.08	10.2	1.62	1.05	0.519
Nb	10.9	3.8	8.8	8	6.9	4.6	2	9.79
Ta	0.75	0.41	0.55	0.49	0.47	0.26	0.15	0.603
La	41.8	16.5	22.8	23.5	57.1	7.11	6.26	14.3
Ce	87.8	30	41.4	38.2	90.4	10.4	8.57	35.11
Pr	10.3	4.13	5.37	4.69	11.9	1.4	1.38	4.77
Sr	103	50	60	77	519	327	295	239.3
Pb	8	<5	19	6	12	<5	<5	<5
Nd	39	15.8	21.1	16.7	47.8	5.48	5.47	22.74
Sm	8.04	3.46	3.33	3.11	9.47	1.07	1.09	6.381
Zr	175	98	124	100	26	79	26	183
Hf	4.4	2.2	2.6	2.2	0.8	1.8	0.6	4.142
Eu	1.88	0.862	0.701	0.619	2.13	0.238	0.254	2.081
Gd	6.96	3.67	2.66	2.61	10.1	0.96	1.15	7.452
Ho	1.26	0.67	0.53	0.52	1.79	0.25	0.22	1.42
Dy	6.44	3.35	2.62	2.67	8.7	1.15	1.11	7.332
Er	3.59	1.94	1.56	1.7	5.08	0.84	0.6	3.871
Tb	1.09	0.58	0.43	0.44	1.49	0.18	0.19	1.221
Y	35.1	21.7	16	18.3	70.5	7.9	8.3	38.39
Tm	0.512	0.272	0.265	0.277	0.677	0.145	0.087	0.551
Yb	3.41	1.79	1.8	1.81	3.97	1.05	0.57	3.512
Lu	0.526	0.282	0.267	0.278	0.547	0.165	0.09	0.516
Co	22	5	9	8	7	3	2	45.53
Cr	110	80	220	150	170	110	30	68.42
Ni	60	60	200	140	80	40	<20	42.63
Zn	100	120	750	660	180	70	<30	127.4
Cu	80	30	150	80	80	50	20	238.9
Sc	23	7	12	10	10	6	2	39.53
V	195	71	2748	1560	190	128	38	410.5
Ga	24	7	20	29	11	7	3	21.84
Sb	0.8	0.2	4.1	2.9	0.9	1.2	0.2	<0.2
Sn	6	<1	2	1	<1	<1	<1	1.1
W	7	8.1	12.4	10	13.9	7.7	11.8	<0.6
Ag	<0.5	<0.5	<0.5	<0.5	<0.5	<0.5	<0.5	<0.5
As	8	11	<5	8	11	6	9	<5
Be	3	1	2	3	2	1	<1	1
Bi	1.2	<0.1	<0.1	0.1	0.1	<0.1	<0.1	<0.1
Tl	0.37	0.4	<0.05	<0.05	<0.05	<0.05	<0.05	0.096
Ge	2	1.6	3.4	7.8	1.1	0.8	<0.5	1.28
Mo	3	4	66	38	3	3	2	<2
In	0.3	<0.1	<0.1	<0.1	<0.1	<0.1	<0.1	<0.1
<b>ppb</b>								
Ru		<dl	0.4997	0.1481			<LoD	0.1755
Rh		<dl	0.3351	0.1765			<LoD	0.4437
Pd		<dl	5.913	2.182			<LoD	8.985
Os		0.2178	0.4457	0.2957			<LoD	<dl
Ir		<dl	0.1178	<dl			<LoD	0.0569
Pt		0.3638	6.861	3.362			0.1818	6.860
Au		0.5354	10.141	2.916			<LoD	2.149
δ <sup>13</sup> C ‰ VPDB	-24.38	-22.62	-24.68	-22.63	-19.07		-1.74	
δ <sup>18</sup> O ‰ SMOW	11.59			14.93			22.03	6.55
δ <sup>34</sup> S ‰ VCDT	12.5	-36.89	-9.77	-2.705	-5.71		-12.28	-1.436

Note: Rock type: m/s—silty mudrock; m—mudrock; mh—hornfelsed mudrock; p/s—silty phosphorite; c/s—calcareous siltstone; c—carbonate. The average Hare Sill diabase analysis (n = 19) excludes S-rich contacts. Areas: SP—Schei Point; BM—Blue Mountains; SHF—South Hare Fiord. Stable isotope data relative to: VPDB—Vienna Pee Dee Belemnite; SMOW—standard mean ocean water; VCDT—Vienna—Canyon Diablo troilite. <dl—below detection limit; LOI—loss on ignition; LoD—limit of detection.

### Raman Spectroscopy

Analyses were done at Western University, Ontario, using a custom-built micro-Raman spectroscopy system that uses a Coherent Innova 90C Ar<sup>+</sup> laser with a wavelength of 514.5 nm as an exciting source. The spectrum is collected in the backscattered geometry and directed to a 500-mm focal length SpectraPro spectrometer using an 1800 grooves/mm grating and analyzed by a liquid-nitrogen cooled charge-coupled device. The collection time for each spot varied between 30 s and 120 s with five iterations, making the total time between 150 s and 600 s. Each iteration was stacked and averaged to reduce the noise in the spectrum. For each sample, five different points across the face of the thin section were probed. Therefore, the total collection time for each sample was ~12.5–50 min.

For low-order graphitic carbon, five Raman peaks located at ~1235 cm<sup>-1</sup> (D4), ~1335 cm<sup>-1</sup> (D1), ~1450 cm<sup>-1</sup> (D3), ~1580 cm<sup>-1</sup> (G), and ~1610 cm<sup>-1</sup> (D2) can be observed, but it is not necessary to observe all of them. In this study, the full width at half of the maximum amplitude (FWHM) of the D1 peak was used to calculate the temperature. Calculated temperatures and uncertainty estimates are provided in Table 4 (see below). Based on the report of Kouketsu et al. (2014), the FWHM of the D1 peak used to calculate low-temperature (<400 °C) graphitic material is shown in Equation 1:

$$T (^{\circ}\text{C}) = -2.15 \times (\text{D1 FWHM}) + 478. \quad (1)$$

### Pyrolysis

Samples were run using a Vinci Technologies Rock-Eval VI analyzer equipped with a total organic carbon (TOC) analysis module at the Geological Survey of Canada, Calgary. Samples were pulverized to pass a 75- $\mu\text{m}$  sieve. Approximately 70 mg of each sample was first heated to 300 °C for 3 min in a helium atmosphere to volatilize free and adsorbed naturally occurring hydrocarbons. The resulting gas was measured as the S1 parameter (mg HC/g rock). The temperature then increased at a rate of 25 °C/min to 650 °C, leading to the thermal cracking of kerogen and subsequent release of hydrocarbons. The gases resulting from this process were measured as S2 (mg HC/g rock), organic-sourced CO<sub>2</sub> (measured as S3; mg CO<sub>2</sub>/g rock), and a portion of mineral-sourced carbon (S3', mg CO<sub>2</sub>/g rock). The amount of hydrocarbon volatilized and evolved from kerogen was measured using a flame ionization detector (FID). Following pyrolysis, samples were moved to an oxidation oven, where the temperature was increased from 300 °C to 850 °C at a rate of 20 °C/min. This phase oxidized any residual organic carbon (S<sub>4</sub>, mg CO<sub>2</sub>/g rock) and the remainder of min-

eral-sourced carbon (S5, mg CO<sub>2</sub>/g rock). TOC content was calculated by adding pyrolyzable organic carbon (PC%  $\approx$  S2 + S3; see Lafargue et al., 1998) and residual organic carbon (RC%  $\approx$  S4). Hydrogen index (HI = 100  $\times$  S2/TOC, mg HC/g TOC), and oxygen index (OI = 100  $\times$  S3/TOC, mg CO<sub>2</sub>/g TOC) were also calculated. The accuracy and precision of pyrolysis parameters were determined through use of a reference standard prepared from the Second White Specks Shale (Ardakani et al., 2016). Measured parameters deviate by less than 5% from the reference. Results are provided in File S5.

### Organic Matter Reflectance

Samples were prepared as polished blocks using a cold-setting epoxy-resin mixture. Petrographic analysis was carried out using a Zeiss Axio Imager II microscope system equipped with white light sources and the Diskus-Fossil system for reflectance measurements carried out under oil immersion using an ultrafine measurement probe (spot size of 0.3  $\mu\text{m}^2$ ). The standard used for reflectance measurements was yttrium–aluminum–garnet with a standard reflectance of 0.906% under oil immersion. Results are provided in File S5.

## RESULTS

### Petrography

Black to dark gray, finely laminated mudstones have local slump structures and generally contain <10% silt-sized quartz and plagioclase, with lesser proportions of altered mafic grains, chert, and opaques (Figs. 4A and 4B). Silty layers contain greater proportions of the same detrital grain population. Fine-grained siliciclastics from the Blue Mountain section have significantly more detrital quartz (reflected in higher bulk SiO<sub>2</sub> contents, see below). Rare muscovite flakes may be detrital. Very fine-grained rounded oxides (1%–3%) are ubiquitous (Figs. 4D and 4E). Most appear to be Fe–Ti–oxide grains, but reconnaissance analyses detected high-Cr# chromite (Table 2) in a Murray Harbour Formation sample.

Anhedral diagenetic pyrite is ubiquitous, typically inclusion-rich, and ranges from very low (<1%) to abundant (>10%; Fig. 5D). Anhedral pyrite is commonly overgrown by faceted pyrite near sills (Fig. 5F). In a few samples, magnetite coronas on pyrite suggest late oxidation. Most samples have amoeboid blebs and veinlets of organic matter (comprising up to several %) that wrap around detrital grains (Figs. 4E–4G). These are especially prominent in the Murray Harbour Formation. Turbid “opaque” platelets (5%–15%) may be disrupted argillaceous laminae (Fig. 4A).

A few samples have very fine carbonate-rich laminae, likely micro-turbidites (Fig. 4C). Well-preserved flattened pelecypod (15 cm wide) fossils are visible on some bedding planes in the Murray Harbour Formation (Fig. 3C), only a few meters under the Hare Sill contact, but fossils are generally scarce. XRD data imply that the clay mineral dickite, chlorite, and/or vermiculite are present.

Sandstones generally have the same clastic components as finer-grained sediments, with dominant quartz > plagioclase > mafics > opaques (Fig. 4B). Turbid, opaque platy clasts comprise ~10%–30% of some samples. These may represent mudstone intraclasts, and/or have the same origin as the opaque platy clasts in the siltstones (disrupted argillaceous layers).

In the South Hare Fiord section, there are subordinate (5%, 10–40-cm-thick), pale carbonate-rich interlayers in the dominant mudstone-siltstones (Figs. 3B and 3D). At one end of the spectrum, calcisiltite limestones (SiO<sub>2</sub> < 7%; e.g., 15BEB-55H in Table 3) are dominated (~80%) by equant, blocky calcite grains (<0.05 mm) that are separated by narrow turbid septa of muddy sediment or organic matter. Other calcareous layers (Fig. 4H) have fewer carbonate grains (<60%) and a siltier matrix (bulk SiO<sub>2</sub> = 20–30%; e.g., 15BEB-60E in Table 3). Minor diagenetic pyrite is common, but larger proportions of coarser cubic pyrite are present near late carbonate veins. The carbonate layers contain a detrital silicate + oxide grain population similar to that of the siliciclastic rocks (~10%, mostly quartz, plagioclase, and Fe–Ti oxides). Geochemical data revealed the presence of P<sub>2</sub>O<sub>5</sub>-rich layers in the Murray Harbour Formation sequence (Table 3), but these samples were too friable to make thin sections.

Host metasediments are typically bleached to a pale gray or tan color for 1–2 m near sill contacts (Fig. 3F) and commonly contain 1–2 mm of euhedral-prismatic contact metamorphic phases (cordierite pseudomorphs? Figs. 3G and 5A–5D). These porphyroblasts are concentrated in clay-rich laminae (Figs. 5A–5D), which implies a local bulk-compositional control. Cruciform-twinning chialstolite/andalusite (Fig. 5E; sample 15BEB-32D) was observed in the Blue Mountains section. Detrital opaque oxide minerals may have core-rim zoning. Some contact-proximal rocks contain pyrrhotite + chalcopyrite rather than pyrite, which suggests a contact metamorphic origin (cf. Deegan et al., 2022). XRD data suggest the occurrence in some thermal aureoles of diopside and garnet, but their presence could not be verified optically.

The lower contact and first meter of section of the Hare Sill is commonly marked by prominent sulfide coatings on joint surfaces (Fig. 3E) and the development of replacive pyrite nodules

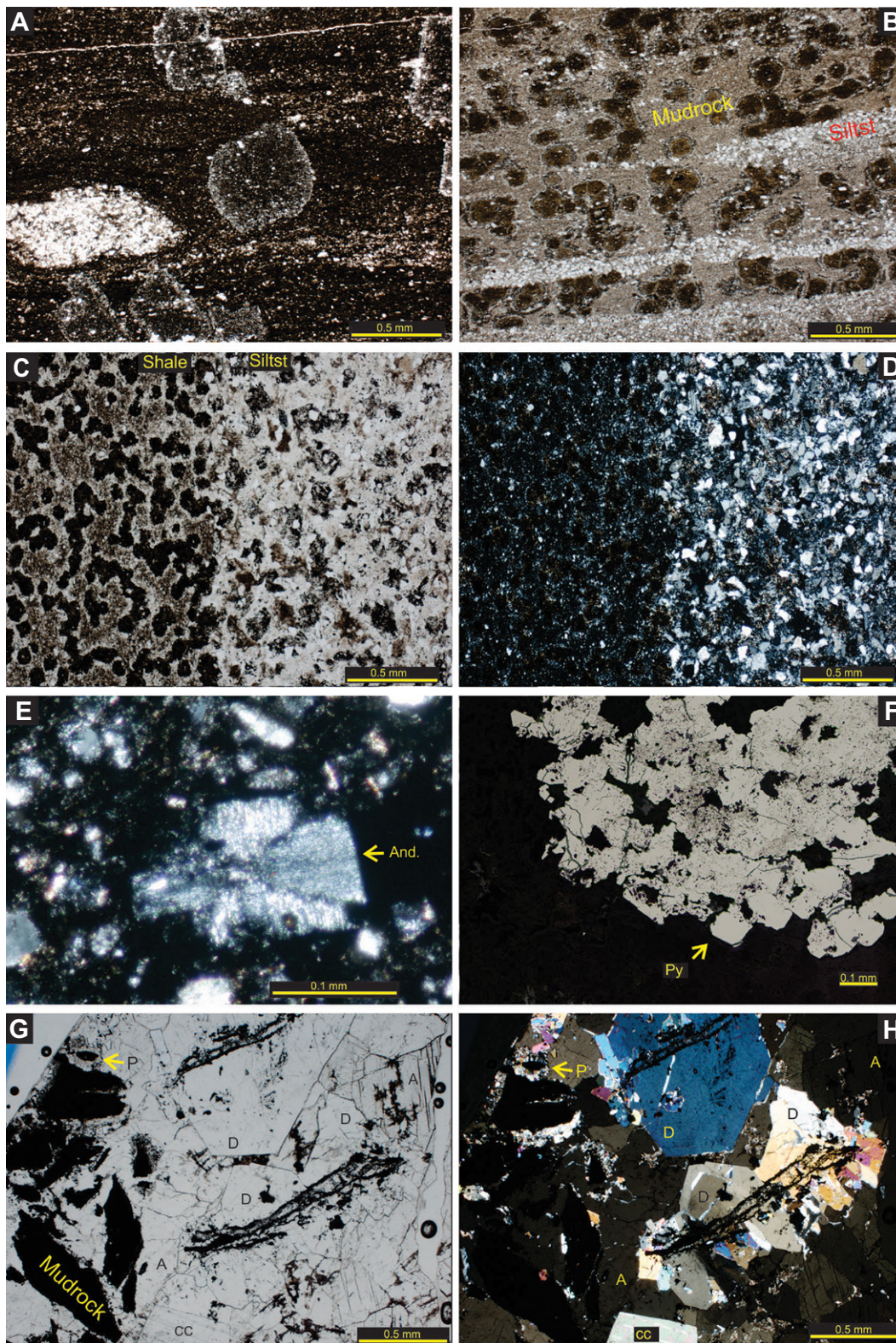


**Figure 5.** Photomicrographs of representative contact metamorphic rocks samples. (A and B) Porphyroblastic hornfels from Heiberg Formation silty mudstones, samples 15BEB-3 and 15BEB-7B, respectively (Schei Point Section). Crossed Nicols. Note how porphyroblasts are concentrated in mudstone laminae, whereas siltstone laminae (labeled Siltst) lack them. (C and D) Transmitted light and crossed Nicol views of contact-metamorphosed silty mudstone from the Blaa Mountain Group (North Geodetic Hills section), sample 15BEB-27B. Sample is located ~1 m from sill contact. Note how porphyroblasts are concentrated in mudstone laminae because of higher Al content. (E) Small andalusite (And.) porphyroblast developed in mudstone, sample 15BEB-32D, Blaa Mountain Group (Blue Mountains Section). (F) Faceted pyrite (Py) overgrowing inclusion-filled diagenetic pyrite in a silty mudstone septum (<1 m thick, sample 15BEB-29B) sandwiched between two sills in the Blaa Mountain Group (North Geodetic Hills section), viewed in reflected light. (G and H) Transmitted light and partly crossed Nicol views of a vein cutting the contact hornfels (sample 15BEB-58C) of the Murray Harbour Formation. The dark patches are mudstone fragments from the host, with some surrounded by prismatic prehnite (P). The vein core here is occupied by euhedral calcite (CC) and datolite (D), surrounded by near-isotropic apophyllite (A).

in the sill itself (Deegan et al., 2018). A pale centimeter-sized leucocratic vein (in sample 15BEB-58C) from within the hornfelsed mudstone below the Hare Sill contains quartz and calcite at the edges, but has a core filled with

euhedral calcite, prismatic datolite (Ca-hydroborosilicate), and apophyllite (F-K-rich, Al-poor Ca-hydro-silicate), with prehnite forming coronas on mudstone fragments (Figs. 5G and 5H; see Table 2 for electron-probe analyses). The

existence of these vein minerals implies that B and F in the sedimentary rocks, possibly derived from diagenetic calcite (Uchikawa et al., 2017), were also remobilized by sill emplacement. However, reconnaissance analyses on three

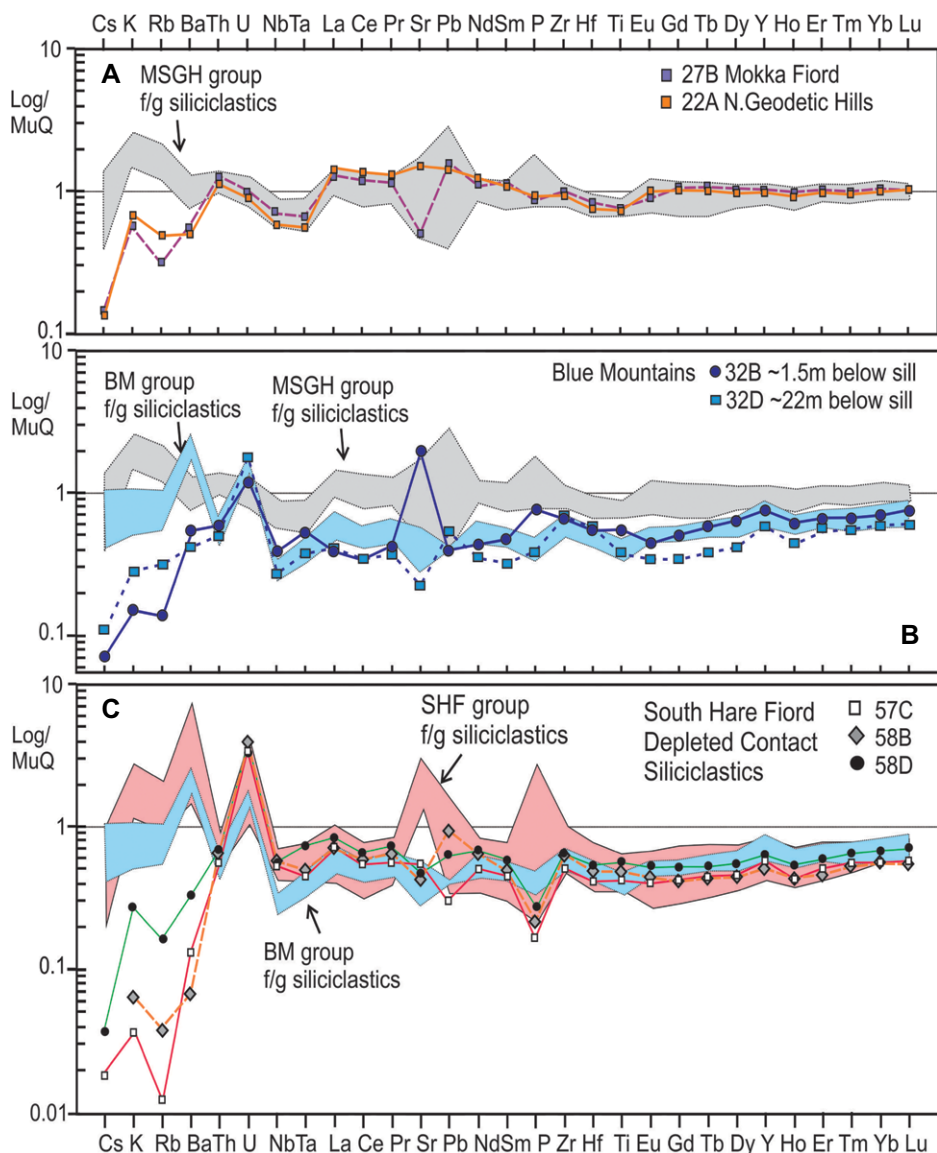


**Figure 6.** Trace element patterns of mudstones and siltstones normalized to Mud of Queensland (MuQ; Kamber et al., 2005). The fields enclose profiles of “normal” samples, with symbols and lines showing anomalous contact-proximal samples depleted in Cs-K-Rb-Ba. (A) Mokka Fiord, Schei Point, North Geodetic Hills, North Hare Fiord (MSGH) group, and sample 15BEB-35B from the Blue Mountains. (B) Blue Mountains (BM) group. (C) South Hare Fiord (SHF), Murray Harbour Formation group. Note the prominent positive Ba-U-Sr peaks of the SHF data, with P-peaks marking a gradation to phosphorites. Very few samples show any trace element depletion, and only the most labile incompatible elements (Cs-K-Rb-Ba) seem to have been preferentially lost.

mudstone samples (15BEB-59G, 15BEB-61i, and 15BEB-63) showed only “normal” sedimentary B (74.5 ppm), Br (1.4 ppm), Cl (140 ppm), and F (767 ppm) contents.

#### Whole-Rock Geochemistry: Major and Trace Elements, Carbon Isotopes

The geochemistry of the sedimentary rocks was examined primarily to see if there were

systematic changes with respect to distance from intrusive contacts. Background samples on figures are simply convenient empirical groupings of local data meant to provide a baseline to detect mobilization of partial melts or fluids. Representative data are provided in Table 3, with the complete data set and geographic coordinates in File S4.

Fine-grained siliciclastics with intermediate  $\text{SiO}_2$  (52–65%; Table 3) from Mokka Fiord,

Schei Point, North Geodetic Hills, North Hare Fiord (labeled the MSGH group in Fig. 6), and a siltstone from the Heiberg Group in the Blue Mountains section (sample 15BEB-35B) all have very similar (Fig. 6A) Mud of Queensland (MuQ)-normalized trace element abundance patterns (Kamber et al., 2005). The Blue Mountains samples constitute the BM group as labeled in Figure 6 (except for sample 15BEB-35B), which has notably higher  $\text{SiO}_2$  (>70 wt%; Fig. 7A; Table 3), reflecting a higher proportion of detrital quartz. Despite petrographic evidence for organic matter (Fig. 4E) and an oily sheen on some rocks, the MSGH and BM group rocks all yielded total organic carbon (TOC) of <2 wt%, with most having <0.5 wt% TOC (Fig. 7). The South Hare Fiord siliciclastics from the Murray Harbour Formation have systematically lower  $\text{SiO}_2$ , higher Cr and Ni, and notably higher TOC (mostly 2–7 wt% TOC; Fig. 7; Table 3). Some phosphoritic South Hare Fiord samples have high  $\text{P}_2\text{O}_5$  (2–5 wt%; Table 2), whereas calcareous layers have  $\text{SiO}_2$  of <30% (Fig. 6A),  $\text{Al}_2\text{O}_3$  of <5.5% (Table 3), and high MgO and CaO contents (Figs. 7B and 7D), which implies the presence of dolomitic components in addition to calcite.

In comparison to sill-distal “background” samples, the vast majority of bleached proximal samples showed no difference in terms of major elements, trace elements, or C-isotope signature (Figs. 6–8). Only seven samples from the rocks examined (15BEB-22A, 15BEB-27B, 15BEB-32B, 15BEB-32C, 15BEB-57C, 15BEB-58B, and 15BEB-58D) showed depletion of trace elements compared to the local background population, with only the most labile elements (Cs-K-Rb-Ba) being lost (Fig. 6). In other respects, these Cs-K-Rb-Ba-depleted samples are almost indistinguishable from the background samples (Fig. 6). The clear implication of these geochemical data is that high-temperature contact metamorphism did not trigger anatexis and that most incompatible trace elements remained immobile. Only the most labile large ion lithophile elements were preferentially removed from some contact-proximal hosts, but not from others. Notably, plots of  $\delta^{13}\text{C}$  and TOC wt% for the detailed sections show no systematic change versus distance to intrusive sill contacts (Fig. 8). However, as discussed below, this lack of change in measured TOC does not imply that the organic matter was unaffected by thermal metamorphism.

#### Contact Metamorphic Minerals

There are no diagnostic metamorphic minerals among our samples that can be used to quantify pressure, but XRD results indicate the presence of high-temperature metamorphic

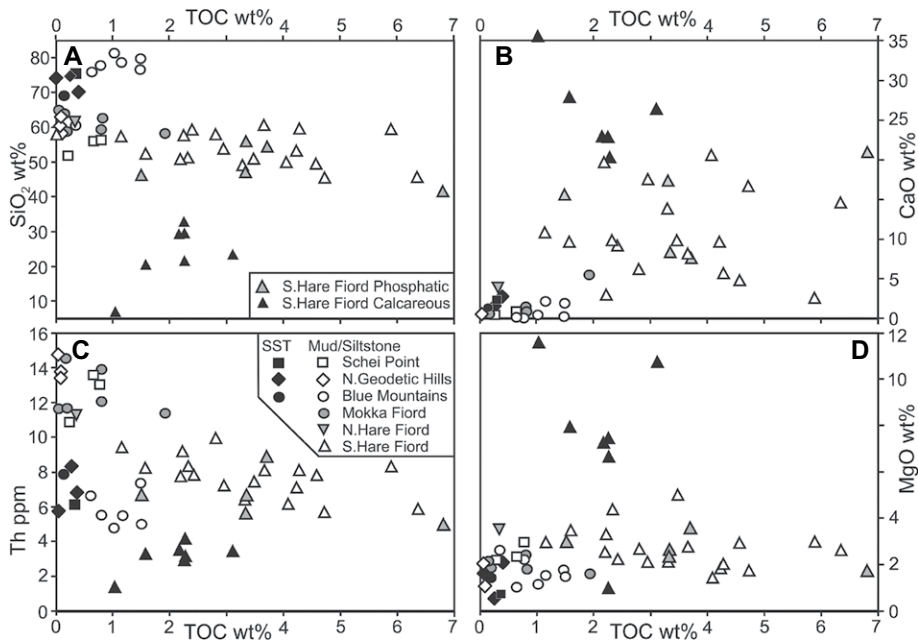


**Figure 7.** Total organic carbon (TOC) in wt% versus (A) SiO<sub>2</sub> (wt%), (B) CaO (wt%), (C) Th (ppm), and (D) MgO (wt%). Note that legend is split between panels A and C. Note high TOC of Murray Harbour rocks from South Hare Fiord.

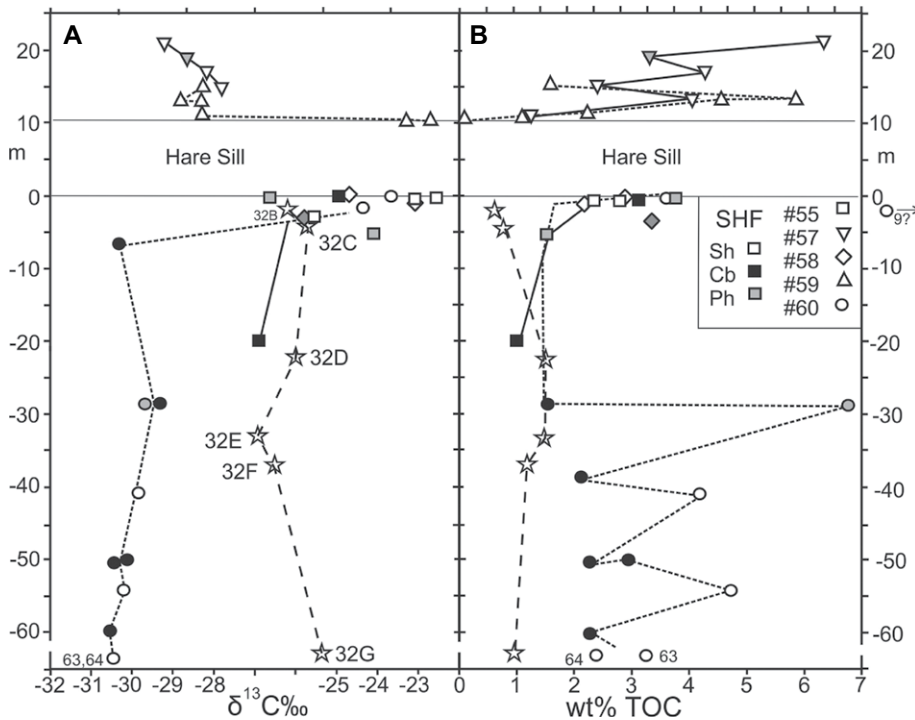


**Figure 8.** (A)  $\delta^{13}\text{C}\text{‰}$  (Vienna Pee Dee Belemnite) and (B) wt% total organic carbon (TOC) plotted versus stratigraphic height. SHF—South Hare Fiord. The different sample sections have distinct symbols, which are coded depending on whether they are “normal” fine-grained siliciclastics (Sh), calcareous (Cb), or phosphatic (Ph). The sample traverse from station 15BEB-32 in the Blue Mountains section (van Hauen Formation) is also shown as stars. The Hare Sill is 17 m thick but is shown as being 10 m thick here to emphasize the host rocks. Note that while some of the Murray Harbour Formation samples have less negative  $\delta^{13}\text{C}\text{‰}$  near sill contacts, the zone affected is extremely narrow, and the TOC content remains high, even at the contact.

minerals in the vicinity of sill contacts (Files S2 and S3). In the Blue Mountains section, andalusite (sample 15BEB-32D, 22 m) and possible cordierite (sample 15BEB-32B, 2 m) were identified from XRD data. We suspect the common porphyroblast pseudomorphs (Figs. 3G, 5A, and 5B) were originally cordierite, but its presence could not be verified optically. If cordierite was present, this suggests equilibration temperatures of 450–550 °C at 1 kbar (Spear and Cheney, 1989) or a slightly higher temperature if formed at higher pressures. The high temperature ( $T > 350$  °C in the KFLASH system; Spear and Cheney, 1989) implied by the presence of andalusite in sample 15BEB-32D is not reflected in the Raman data, which yields 333 °C  $\pm$  5 (Table 4). A possible reason for this is reduced activity of H<sub>2</sub>O in the metamorphic system during heating (Fig. 9), which is supported by the abundance of carbonaceous material and common presence of calcite. Direct experiments and modeling by Deegan et al. (2022) imply that very high-temperature fluids that equilibrated with magma would be dominated by carbon-bearing gases (e.g., CO<sub>2</sub>  $\gg$  CO, CH<sub>4</sub>). Figure 9 shows the temperature sensitivity of various andalusite-producing reactions at 1 kbar to the fluid composition (calculated with the thermodynamic data of Holland and Powell, 2011), which indicates that andalusite-producing reactions can occur at 333 °C in equilibrium with fluids that contain roughly equal molar proportions of H<sub>2</sub>O and CO<sub>2</sub>.

South Hare samples 15BEB-55C (calcareous, 12 cm from contact) and 15BEB-57B (at contact) yielded XRD peaks consistent with grossular garnet, and diopside + quartz, respectively. The diopside + quartz assemblage is consistent with  $T > 450$  °C for systems with  $X_{\text{H}_2\text{O}} = 0.1\text{--}0.8$  at 1 kbar in an H<sub>2</sub>O–CO<sub>2</sub> system (Skippen, 1974). The presence of calcite and dolomite in more distal sedimentary rocks suggests that these minerals would likely have been available to produce contact-metamorphic diopside. Phlogopitic mica is recorded in the XRD results for sample 15BEB-59E (3 m from contact). Phlogopite would indicate temperatures of  $>500$  °C at 1 kbar (Spear and Cheney, 1989). Sample 15BEB-57C also yielded XRD peaks for prehnite, which was observed in some contact-proximal veins (Figs. 5G and 5H). Prehnite is usually restricted to  $T = 150\text{--}300$  °C at  $P < 2$  kbar in mafic rocks (e.g., Frey et al., 1991) and to  $T < 450$  °C at  $P < 2$  kbar in calc-silicate systems (Liou, 1971). There is evidence for vermiculite in samples 15BEB-59D, 15BEB-E, and 15BEB-G. At pressures of  $<2$  kbar, vermiculite is usually restricted to  $T < 350$  °C (Velde, 1978).

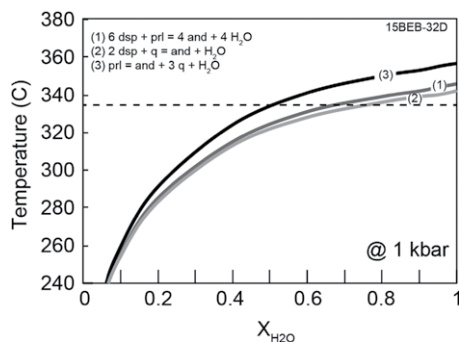


**Figure 9. Temperature in °C versus  $X_{H_2O}$  (molar  $H_2O/[H_2O + CO_2]$ ), showing metamorphic reactions that generate andalusite at low pressure. Dsp—diaspore; prl—pyrophyllite; and—andalusite; q—quartz. Raman thermometry of sample 15BEB-32D ( $\sim 335$  °C) is compatible with fluid compositions of  $X_{H_2O} = 0.5\text{--}0.8$ .**

### Raman Spectroscopy

Given the limited constraints provided by the mineralogical data, and poor resolution of peaks from the XRD analysis, we used Raman thermometry to constrain the thermal halo around High Arctic Large Igneous Province sills. Thermometric results (with uncertainties) are presented in Table 4 and Figure 10. In the Blue Mountains (section at station 15BEB-32), the data show a marked thermal gradient adjacent to a 20–30 m sill, with a peak contact temperature at 407 °C tailing off gradually to a far-field temperature of 265 °C at 33 m distance (for the most distal sample analyzed). The other profiles shown in Figure 10 are sections 15BEB-55, 15BEB-59, and 15BEB-60 from Murray Har-

**TABLE 4. RESULTS OF RAMAN THERMOMETRY VIA RAMAN SPECTROSCOPY OF CARBONACEOUS MATERIAL**

Sample	Temperature (°C)	Error (°C)	Distance from contact
15BEB-32B	407	5	1 m
15BEB-32C	390	5	4 m
15BEB-32D	333	5	22 m
15BEB-32E	265	2	33 m
15BEB-55A	334	6	<2 cm
15BEB-55B	344	29	<2 cm
15BEB-55D	353	11	40 cm
15BEB-55E	330	5	50 cm
15BEB-55F	296	5	300 cm
15BEB-59A2	366	5	<2 cm
15BEB-59B	360	9	<2 cm
15BEB-59E	262	4	3 m
15BEB-59F	263	6	3 m
15BEB-59G	257	6	5 m
15BEB-60A	385	10	<2 cm
15BEB-60D1	235	20	28.5 m
15BEB-60E	263	14	38.5 m
15BEB-60G2	258	9	50 m
15BEB-60H	230	14	50.3 m

Note: Results are an average of five analyses on each thin section (and error on this average). Methodology is similar to that in Kouketsu et al. (2014). Each sample section is given a different color.

bour Formation rocks injected by the Hare Sill (Figs. 3A and 8). Hare Sill sections 15BEB-55 (sub-sill) and 15BEB-59 (supra-sill) record high temperatures proximal to the contact, of up to 353 °C for sample 15BEB-55D and 366 °C for sample 15BEB-59A2, with temperatures falling to 296 °C at 3 m (15BEB-55F) and 257 °C at 5 m (15BEB-59G). The extensive 15BEB-60 section yields high contact temperatures of 385 °C, tailing off gradually to a far-field temperature of 230 °C at 50 m distance.

If the far-field temperature estimates of  $\sim 265$  °C from the Blue Mountains site and  $\sim 230$  °C from the Murray Harbour rocks are representative, the apparent regional thermal gradient would range from  $\sim 85\text{--}77$  °C/km (assuming a 3 km depth) to  $\sim 51\text{--}45$  °C/km (assuming a 5 km depth). These are significantly higher than typical regional thermal gradients and indicate either elevated heat flow, perturbation by nearby High Arctic Large Igneous Province intrusions, or both.

### Organic Matter Maturation: Pyrolysis and Organic Matter Reflectance

Organic matter reflectance measurements were taken on 52 samples (File S5). The dominant maceral is isotropic pyrobitumen, with common anisotropic pyrobitumen and rarer inertinite. Pyrobitumen is present in pore spaces, veins, and as thin interconnected networks and brecciated fragments between detrital grains. Coking textures and fibrous mosaic anisotropic pyrobitumen are evidence of extremely high thermal stress (e.g., samples 15-BEB-029B and 15-BEB-30B). The highest reflectance of 7.84% occurs directly at a sill contact in sample 15-BEB-029B, which shows coking textures. Both the reflectance and standard deviation of the reflectance decrease with increasing distance from the sill contact (Fig. 11A). Background values are poorly established in the area, but samples  $>20$  m from sills seem to show no systematic change in reflectance and have a VRo eq% value of  $\sim 2.5\%$ , which translates to a temperature of  $\sim 210$  °C (Nielsen et al., 2017).

Macerals typically have dispersed or multimodal reflectance histograms due to widespread oxidation. Tmax is unreliable in this data set because either S2 values are too low for reliable Tmax estimation (i.e., below 0.35 mgHC/g TOC; Dewing and Sanei, 2009), or Tmax values are much lower than would be expected for the measured reflectance (Fig. 11B). Reflectance shows a paradoxical decrease with increasing temperature (as determined by Raman spectroscopy). Some samples fall close to the predicted T versus VRo% line of Nielsen et al. (2017); but at temperatures higher than  $\sim 265$  °C, reflectance

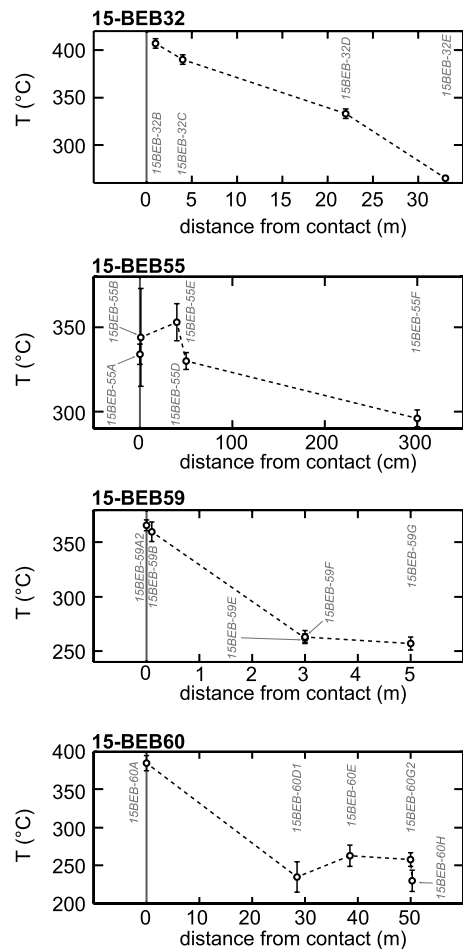


**Figure 10. Results of thermometry via Raman spectroscopy of carbonaceous material in thin section plotted against distance from the contact of intrusion. Error bars are one standard deviation of five analyses from each sample. Intrusion is at left of datum. Blue Mountains profile is at station 15BEB-32. South Hare Fiord profiles 15BEB-55, 15BEB-59, and 15BEB-60 are located in Figure 1A. Note differences in horizontal scale.**

tance decreases (Fig. 11C), possibly due to the creation of nanoporosity (Sanei et al., 2015; Mastalerz et al., 2018). A preferred reflectance value was chosen from multimodal populations by comparison with the reflectance of adjacent samples, comparison to Raman-derived temperatures, and exclusion of either extremely high or extremely low reflectance values.

Rapid heating related to igneous intrusions converted the pyrolysable carbon to (oil/gas) + (residual carbon). When VRo% reaches values of 1.0, over 90% of the TOC consists of residual carbon, and the amount of pyrolysable carbon decreases from 10–100 mg HC/g TOC in immature rocks, to  $<1$  mg HC/g TOC in highly mature rocks (Fig. 12). The loss of pyrolysable

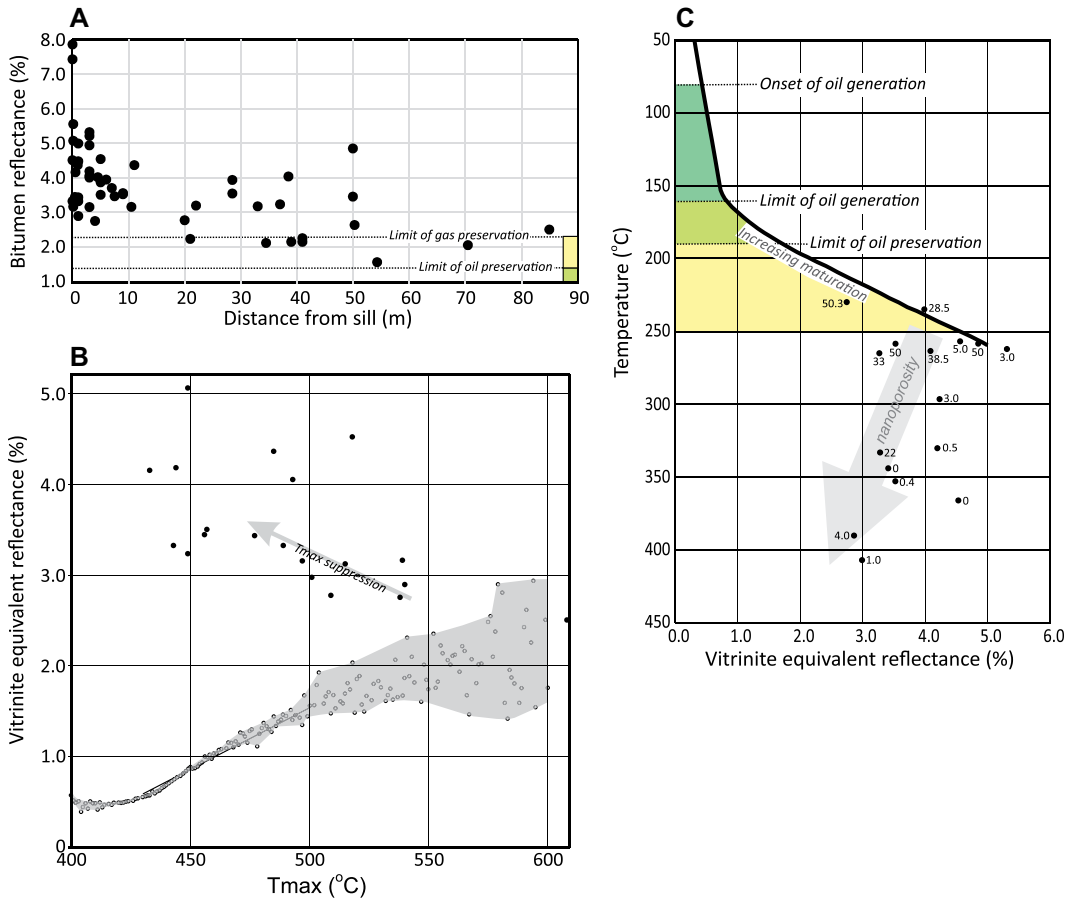


Figure 11. (A) Bitumen reflectance from sill for all samples in this study. Limits of oil and gas preservation were determined using the conversion of bitumen to vitrinite in Landis and Castaño (1995) and vitrinite to temperature in Nielsen et al. (2017). (B) Best-fit curve of median Tmax (°C)-VRo% values from Evnick (2021; gray polygon and open circles) and values from this study with S2 > 0.35 mg HC/g TOC (solid black circles). Tmax is suppressed with increasing reflectance. (C) Temperature determined by Raman (°C) versus vitrinite equivalent reflectance (%). Reflectance appears to decrease slightly with increasing temperature, possibly due to the creation of nanoporosity in organic matter at very high temperatures (see text for details).

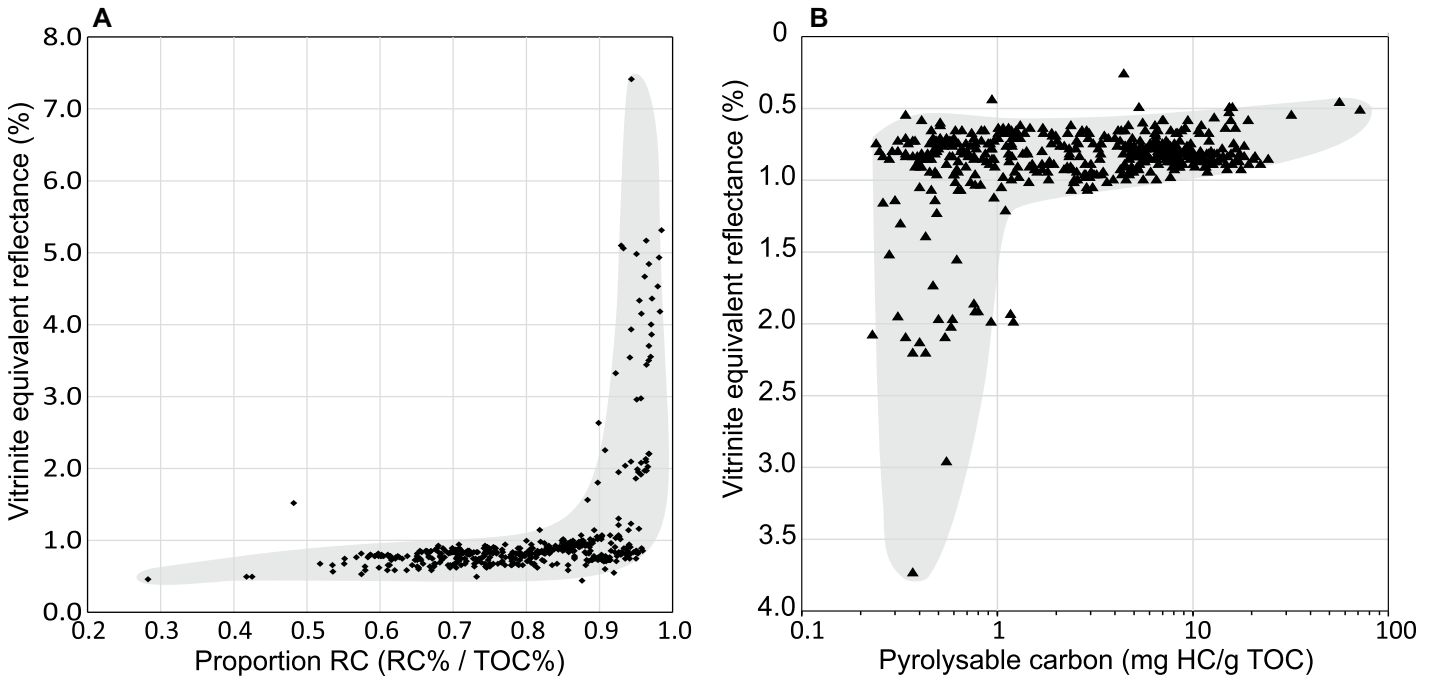


Figure 12. (A) Proportion of residual carbon (RC%)/total organic content (TOC) in samples of Schei Point Group versus vitrinite equivalent reflectance (%). (B) Amount of pyrolysable carbon (mg HC/g TOC) in Schei Point samples versus vitrinite equivalent reflectance (%).

carbon is either due to expulsion of gas or conversion to pyrobitumen.

## THERMAL MODELING

We documented evidence of a thermal aureole created by High Arctic Large Igneous Province sills emplaced in sedimentary rocks that contain organic carbon. To help us interpret these data, we generated a series of thermal models to explore how the temperature field surrounding sills evolved with time.

### SUTRAHEAT Model Approach and Input

The modeling of cooling of sills and heating of their aureoles followed procedures outlined in Nabelek et al. (2012, 2014). Heat conduction was modeled with the finite element program SUTRAHEAT (Nabelek and Chen, 2019). SUTRAHEAT is based on the U.S. Geological Survey SUTRA finite element code (Voss and Provost, 2002) but is focused on modeling heat conduction in igneous and metamorphic environments. The code accounts for latent heat of crystallization and temperature-dependent

thermal conductivity of crystallizing magmas and wall rocks. Thermal conductivity is the product of density, thermal diffusivity, and heat capacity. Coefficients of the temperature-dependent thermal diffusivity and heat capacity functions appropriate for basaltic sills were taken from Nabelek et al. (2012). Properties of melt and solids in magma were considered separately, but were apportioned into single values of conductivity and latent heat at the actual temperature at a grid point during simulation. Density of the crystallized sill was assumed to be 3000 kg/m<sup>3</sup>, and that of wall rocks was assumed to be 2700 kg/m<sup>3</sup>. Density of melt and the nature and fraction of crystals as a function of decreasing temperature were obtained from PELE (Boudreau, 1999) model simulations of Hare Sill crystallization (see below), as these are needed to constrain latent heat addition. Because thermal conductivity of mudrocks and siltstones is highly variable, a constant value of 1.41 W·m<sup>-1</sup>·K<sup>-1</sup> was used. The value is appropriate for silty mudstones with ~30% quartz, which is the most conductive major mineral in these fine-grained clastic rocks (cf. Labus and Labus, 2018).

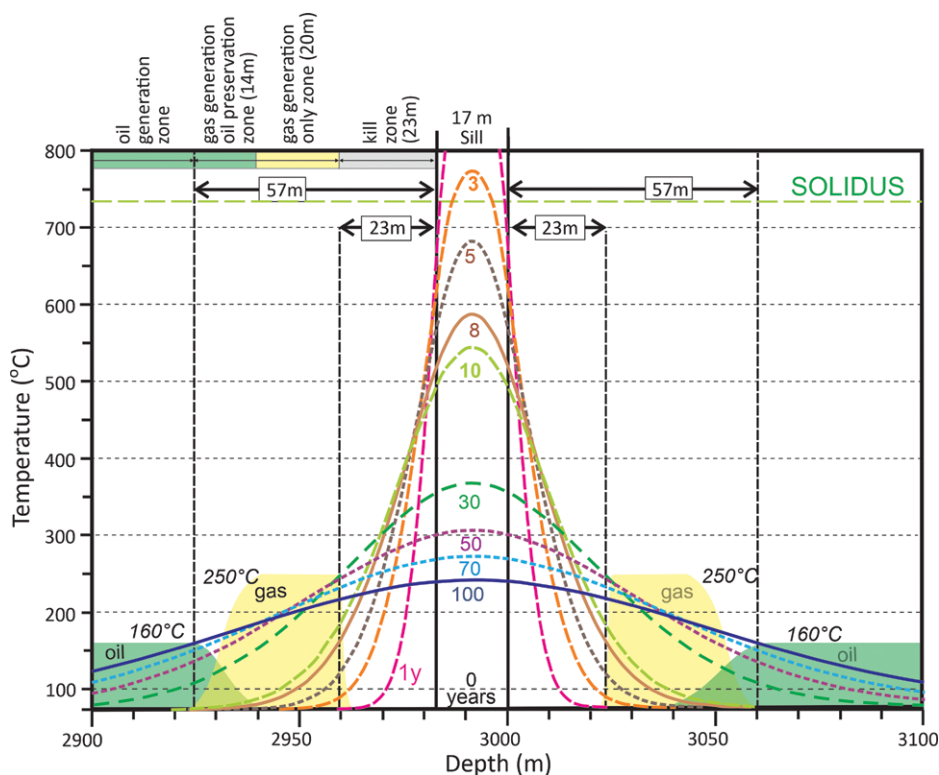


**Figure 13. Isotherms at different times (from 0 years to 100 years after emplacement) from SUTRAHEAT finite element thermal modeling. Model assumes instantaneous emplacement at 3 km depth (range between 2900 m and 3100 m is shown) of a 17-m-thick sill at 1105 °C. The impact on oil and gas generation in the contact metamorphic aureole is shown schematically.**

Despite uncertainty about sill-emplacment age and subsequent erosion, the overburden thickness at the time the High Arctic Large Igneous Province magmas intruded can be estimated for the sites we examined. Jones et al. (2007) inferred a paleo-depth of oil-generating source rocks of the Blaa Mountain Group of ~5 km at 125 Ma, with <1 km of subsidence prior to the emplacement of 95 Ma High Arctic Large Igneous Province sills, and only ~1 km more subsidence prior to the beginning of decompression related to erosional unroofing at 60 Ma. The Depot Point L-24 well used by Jones et al. (2007) is now recognized to contain a fault that repeats part of the section (Dewing and Embry, 2007) and leads to an exaggerated thickness. A new synthesis of drill-hole data produces an estimated burial depth of the middle of the Schei Point Group of 2.7 km at 122 Ma, and 3.4 km at 100 Ma, based on nearby wells (Dewing and Embry, 2007). We consider  $3 \pm 0.4$  km to be the most reasonable estimate of the Hare Sill's emplacement depth. In these wells, thicknesses of units overlying Schei Point are now estimated to be: Heiberg Formation, 1500 m (1438 m in exploration well Sherard P-37); Jameson Bay-Sandy Point formations, 100 m; Ringnes Formation, 50 m; Awingak Formation, 250 m (similar thicknesses were obtained in other exploration wells: Neil O-15, Halcyon O-16, and Romulus C-42); Deer Bay Formation, 200 m (245 m in well Halcyon O-16, 136 m in well Romulus C-42); Isachsen Formation, 150 m (112 m in well Halcyon O-16); and Christopher Formation, 600 m (826 m in well Halcyon O-16, and 557 m in Romulus C-42).

The model basin was assumed to have had an initial "normal" 25 °C/km geothermal gradient, and temperature was held constant at the surface (0 °C) and at the bottom of the domain (150 °C at 6 km) during simulations. Assuming a higher surface temperature would evidently increase the background temperatures at depth by the same amount, but we consider 0 °C to be appropriate for the high latitudes being considered.

The detailed simulation for the Hare Sill in the South Hare Fiord section (Case A; Fig. 13) assumes emplacement at 3 km depth, uses a measured sill thickness of 17 m, and an initial host rock temperature of 75 °C (Fig. 13). The model grid represents depths of between 2500 m and 3500 m. Starting at 2500 m depth (62.5 °C), we used a 10-m spacing to 2880 m, 1-m spacing to 2930 m, 10-cm spacing between 2930 m and 3050 m (this interval includes the sill and the host rocks above and below it), and then 1-m spacing to 3100 m and 10-m spacing to 3500 m (87.5 °C). Although the model grid is two-dimensional, the horizontal orientation of sills



allows for the presentation of results only in the vertical dimension.

As the Hare Sill is a massive I-type intrusion (Latypov, 2003) that shows no evidence of internal differentiation (Bédard et al., 2019), it is assumed to have been emplaced as a geologically discrete event. The Hare Sill averages 5.4% MgO (Table 3) and is representative of the dominant Canadian High Arctic Large Igneous Province tholeiite population (Bédard et al., 2021a). To constrain changes in the latent heat of crystallization contributions as High Arctic Large Igneous Province basalt solidifies, MELTS modeling was attempted (Ghiorso et al., 2002) but did not reproduce the Hare Sill's phases and mineral compositions. The PELE program (Boudreau, 1999), on the other hand, successfully reproduced the phases observed and the High Arctic Large Igneous Province liquid line of descent (LLD) at these pressures for oxygen fugacities of QFM-1 (QFM = relative to quartz–fayalite–magnetite oxygen buffer; see fig. 5 in Bédard et al., 2021a),  $H_2O = 0.7\%$ ,  $CO_2 = 0.5\%$ , and  $S = 0.05\%$ . In the PELE model, the Hare Sill average composition saturates in olivine at 1120 °C and plagioclase at 1115 °C. Petrographic data (Bédard et al., 2019) indicate that the Hare Sill contained 5%–10% antecrysts and phenocrysts, so we infer that the best estimate for the emplacement temperature is 1105 °C (equivalent to 8.3% crystallization prior to emplacement). With further cooling, clinopyroxene co-saturates at 1085 °C (17.1% crystallization), and ilmenite forms between 1045 °C and 1030 °C, but is replaced by magnetite below 1030 °C, with apatite saturating at 955 °C. We assumed a solidus at 730 °C.

A second model (Case B; Fig. 14) has 18 sills with a slightly hotter and more primitive initial melt (1126 °C), with thicknesses of 2 m, 10 m, and 30 m, spaced 100 m apart and emplaced simultaneously between 4000 m and 6000 m depth (Fig. 14). Sill sizes and spacings are similar to those observed in outcrop and wells

(Fig. 2), and the greater depth is more representative of conditions toward the center of the NE Sverdrup Basin. Grid spacing was 10 m from 2000 m to 4000 m, 1 m for the region with sills, and returned to 10-m spacing below 6000 m.

### SUTRAHEAT Model Results

Figure 13 shows the depth range 2900–3100 m, with the base of the Hare Sill at 3000 m. It shows temperature profiles at the time of emplacement ( $t = 0$  years), and for various times thereafter. The modeling yields results similar to those of previous such exercises. Contact-proximal rocks heat up rapidly and attain temperatures of  $>700$  °C for a brief period ( $\sim 1$  year, Fig. 13). By 5 years, the Hare Sill has solidified (730 °C = solidus), and the temperature anomaly collapses rapidly afterward as the thermal pulse propagates outward, with no values  $>550$  °C beyond 10 m distance. By 10 years, all rocks within 10 m of the intrusion are between 450 °C and 400 °C, rocks at 20 m from the contact attain 200 °C, yet far-field temperatures ( $>50$  m) have barely changed from the initial temperature. By 30 years, distal temperatures ( $>100$  m) start increasing and reach a maximum of  $\sim 175$  °C by  $\sim 100$  years after the intrusive event. Host rocks within  $\sim 23$  m of the sill contacts exceed 250 °C where all hydrocarbons are predicted to be destroyed, leaving only residual carbon. Rocks between 23 m and 43 m from the sill contact are in the hydrocarbon gas generation window, those between 43 m and 57 m are in the hydrocarbon gas window but may have preserved oil, and those beyond 57 m are in the oil window.

Case B investigates the thermal impact of emplacing multiple sills with a slightly deeper emplacement depth (between 4 km and 6 km) and higher magmatic temperature (1126 °C; Fig. 14). In this model, the sedimentary rocks halfway between sills reach  $\sim 250$  °C after 100 years, showing that it is possible to raise

regional-scale background temperatures by about  $\sim 150$  °C for the observed High Arctic Large Igneous Province sill density if all sills were emplaced before the previous intrusion's thermal signature had time to dissipate. Rocks situated  $>200$  m from the edge of the sill swarm are largely unaffected. Although we assumed a slightly higher emplacement temperature in Case B, almost identical results would be obtained if the emplacement temperature for the Hare Sill (1005 °C) were used.

### SILLi Modeling

We constrained the volume of gas potentially generated by emplacement of High Arctic Large Igneous Province intrusions to gauge whether these may have had significant palaeoclimatic consequences, and for comparison with other LIPs. Quantification of carbon gas generation and metamorphic aureole processes was performed using the SILLi 1.0 numerical model (Iyer et al., 2018), which recreates the thermal effects of sill emplacement(s) within a sedimentary basin. The model calculates aureole temperatures, vitrinite reflectance, TOC, and the magnitude of generated organic and inorganic carbon gas from contact metamorphism of organic matter (TOC) and marls.

A short description of the model follows, but for full details, see Iyer et al. (2018). The model builds a sedimentary column by depositing sedimentary layers sequentially in time based on the depositional age. The rate of (compacted) sediment accumulation for each layer is determined by its thickness and the difference in time between its top age and that of the underlying layer (File S6). The temperature within the sedimentary column is computed from a prescribed paleo-geotherm (similar to the SUTRAHEAT modeling) and the energy-diffusion equation. This allows us to distinguish the thermal effects of sediment burial from those caused by sill emplacement.

Sills are assumed to be emplaced instantaneously at time zero and then cool by conduction. This provides a reasonable estimate of the thermal structure around a sill, since the effects of fluid flow are largely limited to sill edges. The thermal maturity of the sedimentary rocks is calculated by the EASY%Ro method (Sweeney and Burnham, 1990), and organic carbon generated from the breakdown of organic matter is calculated from the difference in TOC content before and after sill emplacement. The model incorporates a maximum conversion of organic matter to gas of 85% (even within the innermost "hornfels zones") and does not account for interactions between sills and pre-existing accumulations of hydrocarbons. Although it is

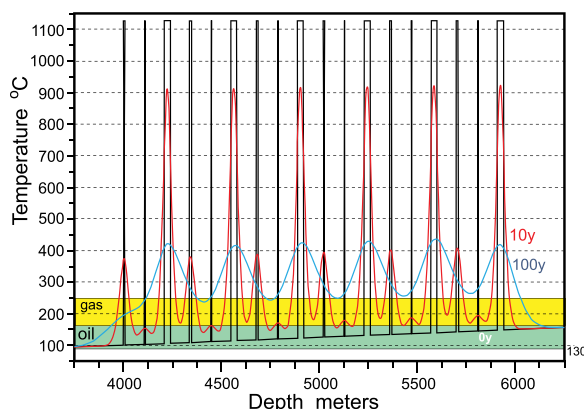


**Figure 14. Forward thermal model assuming instantaneous sill emplacement between 4 km and 6 km depth of a swarm of 18 sills emplaced at 1126 °C. A sill spacing of 100 m was assumed, with sills of 30 m, 10 m, and 1 m thickness. Resulting temperature curves are shown at 0 years (black lines), 10 years (red), and 100 years (blue).**

likely that several C-gas species were generated (mainly CO<sub>2</sub> and CH<sub>4</sub>, but likely also including other C-H-O-S-F-B species), the SILLi model does not account for carbon gas speciation, and outputs are, by default, calculated with all carbon as CO<sub>2</sub>-equivalents.

### Sill-Emplacement Scenarios

In parallel with the SUTRAHEAT modeling, we investigated emplacement of the Hare Sill alone (Case A; Fig. 15), and emplacement of a swarm of 18 High Arctic Large Igneous Province sills (Case B; Fig. 15). All model input data can be found in File S6. Sills in both scenarios were all emplaced at 122 Ma. For Case A, a single 17-m-thick sill was emplaced within the Murray Harbor Formation 500 m below the top of the Blaa Mountain Group. For Case B, 18 sills with thicknesses of 2 m, 10 m, and 30 m were emplaced simultaneously (with a 100 m spacing), covering the full thickness of the Blaa

Mountain Group (Fig. 15). Case A was run with two different initial TOC values for the intruded host rock. Case A-1 assumes a high TOC content of 5.7 wt% for the Murray Harbor (in the upper half of the observed range, Fig. 7) and Blaa Mountain Group. Cases A-2 and B both assume a lower value of 3 wt% TOC, which represents a reasonable average value at the time of deposition for the other units in the Blaa Mountain Group (Obermajer et al., 2007). This will illustrate the contrasting effects of the single-sill versus multiple-sill scenarios, and of different initial TOC contents. Input data regarding the depositional history of the Sverdrup Basin were based on stratigraphic constraints and thicknesses outlined in the section on Forward Modeling, including constraints such as depths/thicknesses/ages of the sedimentary formations, and a paleo-geothermal gradient of 25 °C/km (File S6). Erosion did not affect the temperature of the basin until after the time of sill emplacement as the onset of erosion occurred at 60 Ma (Jones et al., 2007). Eroded layers were not included in the model.

The thermal effects modeled for the sill-emplacment scenarios are shown in Figure 16. The temperature rises from background levels and reaches a maximum of ~720 °C (Case A) and 730 °C (Case B) at the innermost aureoles; these results are comparable to those of the SUTRAHEAT model (see above; Figs. 13 and 14). The TOC contents decrease, and vitrinite reflectance values increase sharply toward the sills. Thermogenic organic CO<sub>2</sub> gas is generated within the aureoles of all sills, with much of the gas produced in the first 20 m of the aureole. Since the intruded Blaa Mountain Group does not comprise any significant deposits of carbonate/limestone, the model did not predict any inorganic thermogenic carbon. Comparing modeled vitrinite reflectance results to present-day vitrinite reflectance measurements from the nearby Gemini E-10 exploration well shows that the slope of the depth versus VRo% curve is well calibrated (Fig. 16A, Case A-1), although there is a slight shift in Gemini E-10 data, which implies a slightly greater depth of burial by Tertiary strata in that area (cf. Bustin, 1986).

Figure 17 shows the cumulative equivalent-CO<sub>2</sub> gas production for the three scenarios, combining the thermal effects of both sediment burial and sill emplacement(s). For all scenarios, the CO<sub>2</sub> production slowly increases from the start of basin formation due to burial, diagenesis, and the maturation of organic matter in the sediments. Deposition of the organic-rich Blaa Mountain Group began at 250 Ma. This unit was given a TOC value of 5.7 wt% for Case A-1, but 3.0 wt% for Case A-2 and Case B. Because of the higher initial TOC, the initial background CO<sub>2</sub>

production is higher for Case A-1 than for Case A-2 and Case B until sill emplacement occurs at 122 Ma. Immediately following sill emplacement at 122 Ma, Cases A-1 and A-2 show an increase in CO<sub>2</sub> production of ~20 tonnes/m<sup>2</sup> and ~10 tonnes/m<sup>2</sup>, respectively. A significantly larger burst of CO<sub>2</sub> production characterizes the multi-sill scenario (Case B, ~226 tonnes/m<sup>2</sup>), which heats a much larger volume of host rock. Thereafter, CO<sub>2</sub> production increases only very slowly in Case B (Fig. 17), because most of the Blaa Mountain Group was stripped of its organic carbon through the emplacement of multiple sills. In contrast, most gas generation in Cases A-1 and A-2 occurs slowly and continues after the High Arctic Large Igneous Province heat pulse subsides. This continued CO<sub>2</sub> production is possible because most of the stratigraphy was unaffected by the narrow thermal halo of the isolated sill (Fig. 16). Case A-1 yields slightly larger cumulative CO<sub>2</sub> production (from both sill heating and burial) than Case B, but this is likely an overestimation, as the average TOC of all of the Blaa Mountain Group rocks was less than 5.7%.

## DISCUSSION

### Thermal Impact of High Arctic Large Igneous Province Sill Swarms

Constraints from mineralogy and Raman thermometry are compared to the forward thermal models in Figure 18. The mineralogical constraints are shown as colored boxes (A = andalusite, D = diopside, G = garnet, and C = cordierite), and Raman temperatures are shown as boxes or ovals. The different approaches are broadly consistent, with high contact-proximal temperatures tailing off to lower far-field temperatures. However, the SUTRAHEAT models yielded far-field temperatures of ~175 °C, whereas the Raman data at these distances are between 220 °C and 300 °C. One possible explanation for the ~50 °C difference is that the average surface temperature was higher than 0 °C, though we consider 0 °C reasonable for a high-paleolatitude setting (~70°N). While it is possible that we under-estimated the depth of emplacement of the Hare Sill by ~2 km, exploration wells in the region give consistent thicknesses for stratigraphic units, and our depth estimate originates from these. A potentially simpler explanation for the apparent excess temperature is that the Hare Sill is part of a sill swarm with overlapping thermal haloes (e.g., Figs. 14 and 16; also see Aarnes et al., 2011). In fact, it is very common to observe swarms of sills in Sverdrup Basin strata (e.g., Schei belt; Williamson et al., 2016; Saumur et al., 2022), where they may make up significant proportions of the section (10%–

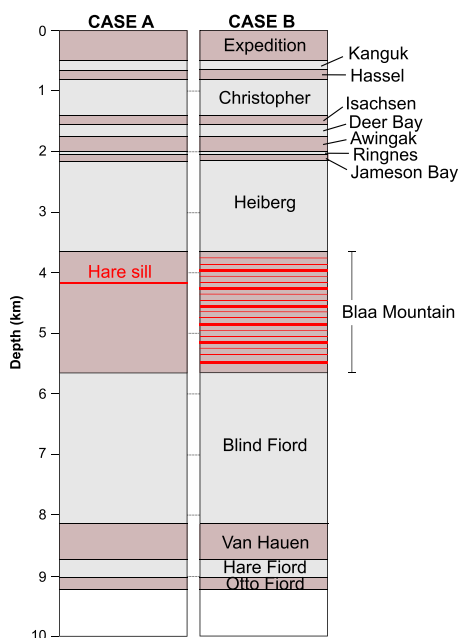


**Figure 15.** Overview of the full Sverdrup Basin sedimentary column (including all major sedimentary formations) used as input for the SILLi model. The two columns represent two different sill-emplacment scenarios: Case A (Hare Sill only) and Case B (High Arctic Large Igneous Province sill swarm). In both scenarios, sills are emplaced within the Blaa Mountain Group. Note that the Christopher, Hassel, Kanguk, and Expedition formations were deposited after sill emplacement (i.e., at 122 Ma). Therefore, the sill depths shown here correspond to the present-day sedimentary column.

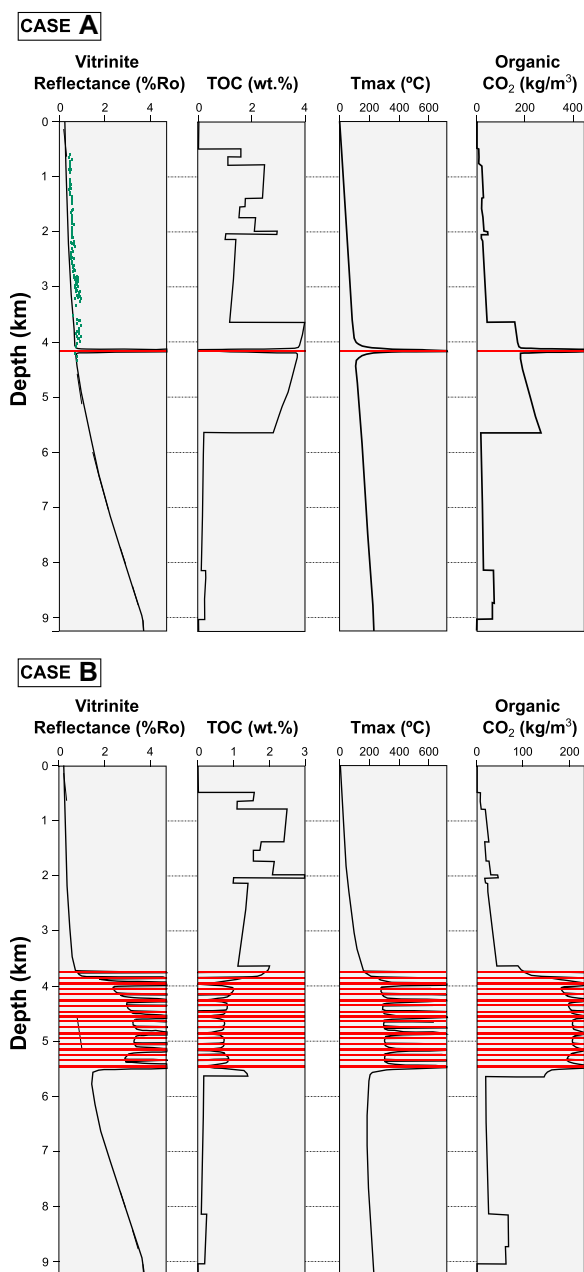


**Figure 16.** SILLi modeling results showing thermal effects of the emplacement of the Hare Sill (Case A) and a High Arctic Large Igneous Province sill swarm (Case B) within the Blaa Mountain Formation in the Sverdrup Basin. (See Fig. 15 and File S6 [see text footnote 1] for detailed model setup.) Maximum temperature and vitrinite reflectance values increase, while the total organic carbon (TOC) content decreases toward the sills. Organic carbon-derived CO<sub>2</sub> gas is generated in aureoles above and below all sills. Case A vitrinite reflectance is compared to measured reflectance in nearby Gemini E-10 well (green squares; Dewing et al., 2007a). The stratigraphy of Gemini E-10 is compared to the model stratigraphy. The well and the model use the base of the Heiberg Formation as datum.

30%; Fig. 2). Thermal modeling of a sill swarm (Figs. 14 and 16) yields temperatures of between 200 °C and 300 °C for all rocks between coeval sills, which match the Raman temperatures. At the South Hare Fiord section (Figs. 1A and 3A), there is a 20- to 30-m-thick, medium-grained sill outcropping to the north that is stratigraphically ~50 m beneath the sampled section. We cannot be certain whether this (and other sills) were coeval with the Hare Sill, but there is geochemical and petrological evidence supporting the notion that the High Arctic Large Igneous Province plumbing system comprised near-coeval sill-swarms and cross-dikes. Geochemical data from the volcanic sections of the Strand Fiord

Formation (Dostal and MacRae, 2018; fig. 29 in Bédard et al., 2021a) imply that geochemically diverse lava flows erupted with few sedimentary intercalations, which implies near-synchronous eruption of magma from multiple shallow and unhomogenized magmatic reservoirs. Mineral chemical data (Bédard et al., 2019) indicate that the Hare Sill, although internally undifferentiated, contains antecrysts that record multiple magmatic mixing events, which also require the existence of multiple, coevally active conduits that regularly intersected and mixed prior to emplacement and possible eruption.

The high-far field temperatures shown by the data and models far exceed a possible 25 °C

increase consequent to estimates of ~1 km further burial after the 122 Ma High Arctic Large Igneous Province pulse (see above). We therefore conclude that the >200 °C temperatures that developed in the Sverdrup Basin sedimentary rocks studied almost certainly reflect a common High Arctic Large Igneous Province thermal footprint, which is likely associated with the emplacement of near-coeval sill swarms associated with lateral magmatic propagation. Although temperature evolution in the Sverdrup Basin affected by High Arctic Large Igneous Province thermal pulses was modeled in a completely different way by Jones et al. (2007), they obtained very similar results.

### Greenhouse Gas Generation by High Arctic Large Igneous Province Magmatism

The full regional extent of sill emplacement in the Sverdrup Basin is uncertain, but sills and sill-swarms are most commonly observed in Triassic

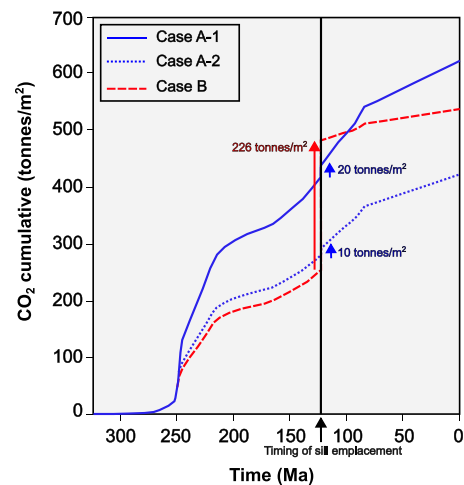


**Figure 17.** SILLi modeling results showing the cumulative generation of organic carbon-derived CO<sub>2</sub> within the Sverdrup Basin since its formation, due to both heating from burial of the sediments and heat transfer from cooling sill intrusions. The timing of instantaneous sill emplacement at 122 Ma is illustrated by the vertical black line. For Case A-1 (blue solid line), the CO<sub>2</sub> production increases from background maturation levels (i.e., ~417 tonnes/m<sup>2</sup>) to ~437 tonnes/m<sup>2</sup> directly following Hare Sill emplacement, giving a total of ~20 tonnes/m<sup>2</sup>. For Case B (red dashed line), there is a much higher jump in thermogenic CO<sub>2</sub> production, from background maturation levels of ~253 tonnes/m<sup>2</sup> to ~479 tonnes/m<sup>2</sup> directly following High Arctic Large Igneous Province sill swarm emplacement (total of ~226 tonnes/m<sup>2</sup>).

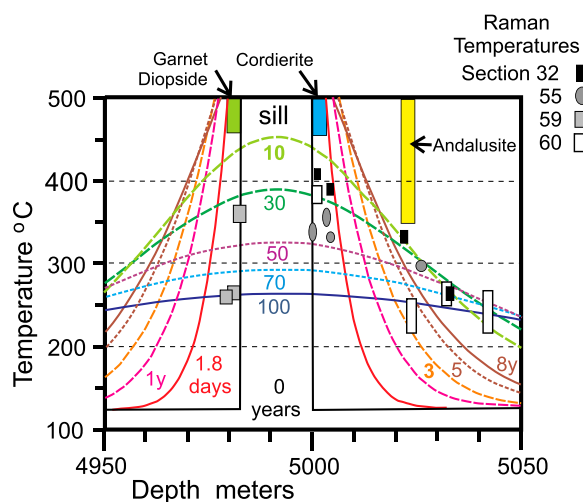


**Figure 18. Constraints from mineralogy and Raman thermometry compared to forward thermal models of Figure 13B. The mineralogical constraints are shown as colored boxes (A—andalusite, D—diopside, G—garnet, and C—cordierite) as discussed in the text. Raman temperatures from Figure 10 are shown as boxes or ovals (encompassing the error bars). Overall, the three approaches yield broadly consistent results, with high contact-proximal temperatures that tail off to far-field temperatures of  $>200$  °C at  $\sim 50$  m from the contact within 100–150 years after the intrusive event, but drop to below 200 °C at this distance 200 years after the intrusive event.**

and Jurassic mudstone + siltstone and sandstone packages (Fig. 1; Saumur et al., 2022). Note that potential gas generation during heating of other sedimentary units in the basin is not included in our estimate. SILLi modeling of the Hare Sill aureole predicts  $\sim 20$  tonnes/m<sup>2</sup> of thermogenic CO<sub>2</sub> (all carbon gas is reported as CO<sub>2</sub>; Case A-1; Fig. 17). Case B assumes multiple synchronous sill-emplacement events in the entire Triassic Blaa Mountain Group (2 km thick, 3 wt% TOC), with the number, thickness, and spacing of the sills resembling sections studied in the Schei sill belt and wells (Saumur et al., 2022; cf. Fig. 2 and Table 1). Case B yields a total CO<sub>2</sub> production of  $\sim 226$  tonnes/m<sup>2</sup> due to the emplacement of the sill swarm (Fig. 17). This value is higher than the gas productivity (per m<sup>2</sup>) of sedimentary basins related to other LIPs calculated by the same model: Siberian Traps = 50–80 tonnes/m<sup>2</sup> (Svensen et al., 2018); Central Atlantic Magmatic Province (CAMP) = 97 tonnes/m<sup>2</sup> (Heimdal et al., 2018); and Karoo = 115–135 tonnes/m<sup>2</sup> (Svensen et al., 2020). The high rate of gas production predicted for the Sverdrup Basin may be due to the great thickness and high TOC of the Blaa Mountain Group source (2 km, 3 wt% initial TOC), but as these values are closely grounded by observations (Figs. 7 and 8; Files S4 and S5), we consider them realistic. A second possible factor is that we assumed instantaneous emplacement of multiple closely spaced sills, which leads to significantly higher gas production than models published for other basins, many of which assumed longer spans of time between intrusions, which allow individual thermal haloes to dissipate (Iyer et al., 2018; Heimdal et al., 2018).

We now extrapolate our estimated values of thermogenic CO<sub>2</sub> production to the basin scale. The intruded part of the Murray Harbour

Formation covers  $\sim 128,000$  km<sup>2</sup> (Fig. 1C). A single 17 m sill of this extent (Cases A1 and A2) would yield up to  $\sim 2550$  Gt of CO<sub>2</sub> (considering a starting host rock TOC content of 5.7 and 3.0 wt%, respectively). If the intruded part of the Blaa Mountain Group is equivalent to the area of 20% intrusion density in Figure 1D (i.e., 56,800 km<sup>2</sup>), the multiple sill model (Case B, 3% starting TOC) would yield  $\sim 13,000$  Gt CO<sub>2</sub>, a value within the range of thermogenic gas release estimated for other LIPs, such as the Siberian Traps, North Atlantic Igneous Province, Central Atlantic Magmatic Province, and the Karoo (e.g., Svensen et al., 2007, 2009; Ganino and Arndt, 2009; Aarnes et al., 2010; Ruhl and Kürschner, 2011; Frieling et al., 2016; Galerne and Hasenclever, 2019). These LIPs are all linked to significant carbon cycle perturbations and major biotic and/or climatic disruptions, including the end-Permian mass extinction, the Paleocene–Eocene thermal maximum, the end-Triassic mass extinction, and the Toarcian crisis. The associated perturbations of the carbon cycle are demonstrated by sedimentary proxy records that attest to significant increases in the atmospheric concentration of CO<sub>2</sub> as well as negative carbon isotope excursions. Combined, these proxy records suggest significant release of <sup>12</sup>C-enriched thermogenic CO<sub>2</sub> and CH<sub>4</sub> gas to the atmosphere. Most of these LIPs are associated with hundreds to thousands of degassing structures evidenced through exposure and/or seismic data, which attests to the release of thermogenic carbon gas generated in their respective volcanic basins (i.e., Tunguska, Vøring/Møre, and Karoo basins).

Our results have important implications for understanding how the High Arctic Large Igneous Province influenced oceanic anoxic events

(OAEs) and the Cretaceous greenhouse climate. Planke et al. (2017) suggested that carbon released from thermally altered sediments could have triggered OAE 1a, and the High Arctic Large Igneous Province has been suggested as the driver of OAE 2 (e.g., Jenkyns et al., 2017; Schröder-Adams et al., 2019). Naber et al. (2021) demonstrate that the main subareal High Arctic Large Igneous Province eruptive events are temporally coincident with both OAE events, and our results show that the High Arctic Large Igneous Province would have generated significant volumes of greenhouse gases, which supports a causal linkage. The subareal eruptive phases of the High Arctic Large Igneous Province would have had especially strong impacts, as greenhouse gases would have been released directly into the atmosphere.

### Effect on Petroleum Potential

Intrusions can either enhance or destroy the petroleum potential of a sedimentary basin (e.g., Jones et al., 2007; Wang et al., 2012; Sydnes et al., 2018; Spacapan et al., 2018; Goodarzi et al., 2019). Temperature estimates from our modeling indicate that much of the hydrocarbon source-rock potential in the Sverdrup Basin was destroyed by High Arctic Large Igneous Province intrusions. Oil is generated between  $\sim 80$  °C and 160 °C (Fig. 13; see Stolper et al., 2014). Oil that is not expelled is destroyed by conversion to pyrobitumen and gas by  $\sim 190$  °C, with thermogenic gas generation taking place between 160 °C and 220 °C from oil- or gas-prone kerogen (Stolper et al., 2014). Gas data from drill cuttings show a decrease in gas concentrations above VRo% of  $\sim 2.5\%$ , which indicates that methane is expelled or destroyed faster than it is created at  $\sim 220$  °C (Dewing et al., 2007b). Overall, hydrocarbon gases are considered to have been largely destroyed or expelled by  $\sim 250$  °C. Applying these temperatures to the modeled 17-m-thick sill in Figure 13, the zone of complete hydrocarbon destruction extends 23 m away from the upper and lower sill contacts ( $2.7\times$  sill width), and the zone of hydrocarbon gas stability extends 57 m away from the upper and lower sill contact ( $6.7\times$  sill width). Oil would only be preserved greater than 43 m from this sill contact (Fig. 13).

Our results are consistent with those of previous work on the Sverdrup Basin (Goodarzi et al., 2019) showing that solid organic matter can be affected up to 3.3 times the sill width, and natural gas composition is altered up to 7.5 times the sill width. Studies of thermal aureoles around Karoo sills show the rate to be generally 1–1.5 times the sill width (Aarnes et al., 2010). However, Wang et al. (2010) and Wang and Manga

(2015) showed that the aureole width above shallow sills is locally controlled by the position of hydrothermal convection cells, and that this can extend the thermal footprint to eight times the sill width in places.

Drilling in the NE Sverdrup Basin intersected a total of 1293 m of Murray Harbour Formation, and 260 m of injected sills within it (20%; Fig. 2A). Based on the zone of complete hydrocarbon destruction being about  $\sim 2.7$  times the sill width (Fig. 13), over half of the hydrocarbon potential of the Murray Harbour Formation would have been destroyed by even a few

isolated intrusions. If the sills were emplaced as swarms with coalescing thermal haloes (Fig. 14), then even more of the Murray Harbour Formation would have been sterilized for hydrocarbon generation. While High Arctic Large Igneous Province intrusions were emplaced prior to maximum burial, the addition of 1.4 km of strata following the High Arctic Large Igneous Province (Bustin, 1986) adds only  $\sim 35$  °C of burial temperature, which is insufficient to raise the temperature of the rocks above those previously generated by High Arctic Large Igneous Province intrusions.

If Murray Harbour Formation strata in the area of High Arctic Large Igneous Province intrusions reached the gas window (Fig. 13), any remaining hydrocarbon potential within the unit would exist as a shale gas resource. But many unknowns remain: how much of the gas that was generated was methane, C2–C4 (ethane to butane), and CO<sub>2</sub>; what proportion of gas was expelled; and what proportion was destroyed. Drill-stem tests from Mesozoic intervals in wells drilled within the intruded area have higher CO<sub>2</sub> than drill-stem tests from Mesozoic intervals outside of the intruded area (1.8 mol%,

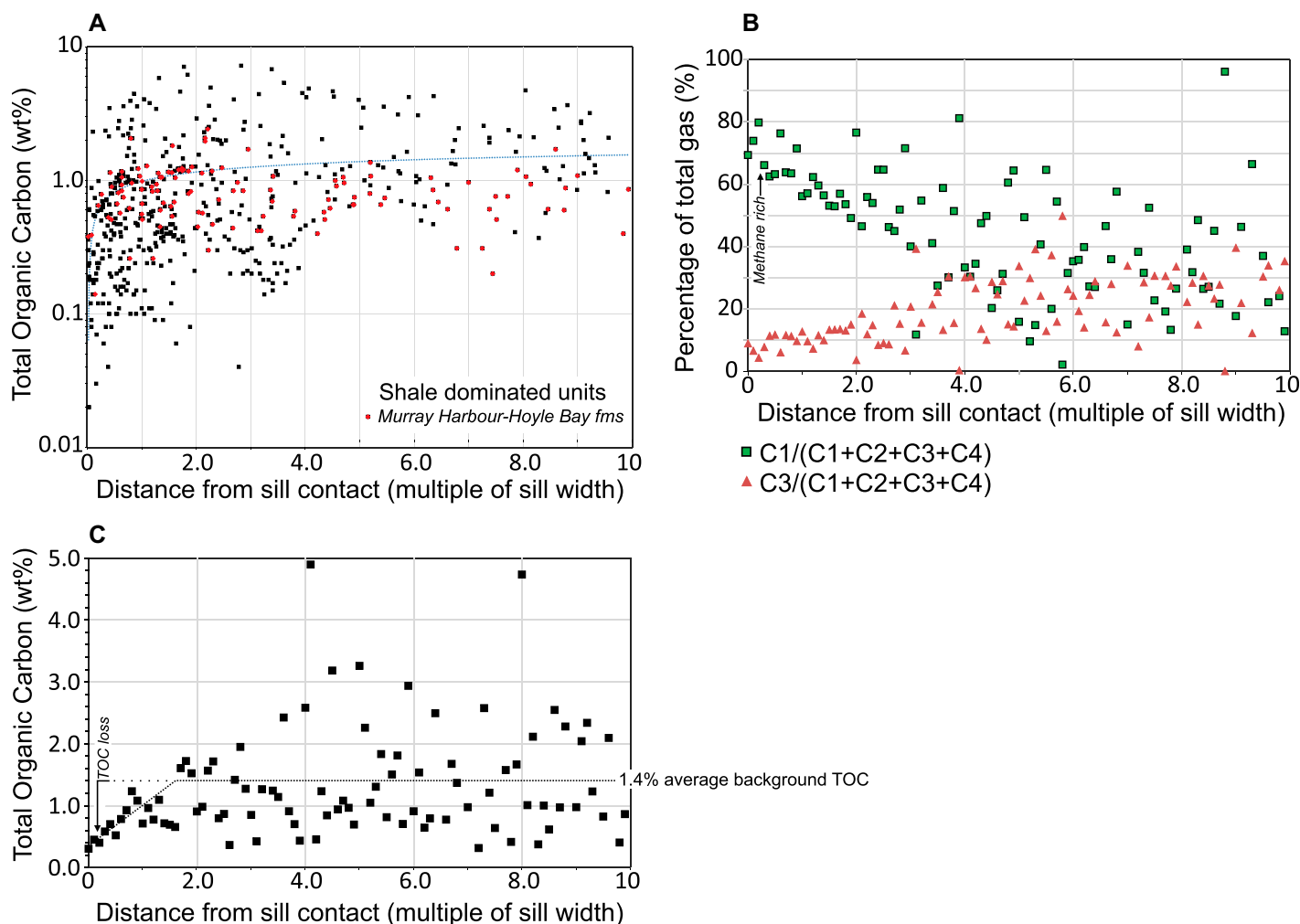


**Figure 19.** (A) Change in total organic carbon (TOC) versus distance from sill contact (expressed as % of sill thickness) for shale-dominated units in well data. Data are from cutting samples from wells (Dewing and Embry, 2007). Red diamonds are samples of Middle Triassic, organic-rich Murray Harbour or Hoyle Bay formations. These show relatively little change in TOC toward the sill margin. Samples within 3 m of a sill were removed because the cutting sample interval (10 ft or 3 m) could overlap with the sill itself and contain igneous material. Samples adjacent to sills that have TOC greater than 0.6 wt% were excluded because the high TOC within the sill is likely due to hydrocarbon that migrated into them post-emplacment. Note the logarithmic scale. (B) Same data as in panel A, but showing average of all data binned by 0.1 multiples of sill width from the sill contact. TOC appears to systematically decline starting at  $\sim 1.8$  times the sill width. (C) Proportion of methane (C1, green squares) and propane (C3, orange triangles), binned by 0.1 m intervals from the sill contact. The proportion of methane increases toward the sill starting at a distance equal to 4 times the sill width. The proportion of propane (C3) decreases toward the sill, which implies that gasses with higher C numbers are being progressively cracked to methane.

$n = 11$  versus 0.5 mol%,  $n = 41$ ; Dewing et al., 2007b), and more C2–C4 gasses (89.4% methane versus 98% methane), with similar nitrogen content (both 2.5 mol%). The data set is small, but consistent with source rocks in the intruded area having produced abundant thermogenic gases and CO<sub>2</sub>.

### How Much Carbon Is Released, and How Much Is Trapped in the Crust?

The mineralogical and thermometric evidence (Figs. 3, 5, 9, and 10) confirms the existence of thermal haloes around High Arctic Large Igneous Province intrusions in organic-rich Sverdrup Basin sedimentary rocks. Our modeling (Figs. 13, 14, and 16–18) predicts near-total conversion of carbon to gas, with essentially all of the original organic carbon being destroyed. Most sites we examined from the Blaa Mountain Group indeed have low TOC (often <0.5 wt%), which is consistent with large-scale carbon loss during heating. Note that at the time of deposition, the Murray Harbour Formation was inherently richer in TOC than the other Blaa Mountain Group units (Obermajer et al., 2007). Data from wells in the Sverdrup Basin show that TOC decreases with proximity to sill contacts, from a background of ~1.4 wt% to 0.3 wt%, or a loss of ~1.1 wt% organic carbon from the thermal aureole extending to 1.6 times the sill width (Fig. 19C). This is consistent with heating related to igneous intrusions having converted the pyrolysable carbon to (oil/gas) + (residual carbon) (Figs. 12A and 12B).

Paradoxically, rocks of the Murray Harbour Formation in the detailed study area still contain large amounts of organic carbon even close to sill contacts ( $\leq 3.6\%$ ; Figs. 7 and 8), which is not easily reconciled with the high temperatures indicated by the direct thermometry (Figs. 9 and 10), mineralogy (Fig. 5 and File S2), and the thermal modeling (Figs. 13, 16, and 18). Potential explanations for this conundrum include the following: (1) The Murray Harbour may originally have had much higher TOC, making the gas volume estimates (Fig. 17) minima, but this does not explain retention of very high TOC near sill contacts (Figs. 7 and 8). (2) The permeability of these organic-rich siliciclastic rocks may have been too low to allow hydrocarbons to escape effectively during the transient High Arctic Large Igneous Province thermal event (cf. Daigle et al., 2019; Zhang et al., 2018; Guo et al., 2022). Gas-escape breccia pipes and vents related to sills are observed by the hundreds to even thousands in the Karoo Basin (Svensen et al., 2020), Tunguska Basin (Siberian Traps, Svensen et al., 2009), and Vøring and Møre basins (North Atlantic Igneous Province; Svensen et al., 2004). In contrast, such

degassing structures are not widely observed in the High Arctic Large Igneous Province, despite excellent exposure, which suggests that widely spaced, isolated faults may represent the only high-permeability gas-escape conduits there. In this scenario, some of the gas generated during the heating of fine-grained Sverdrup Basin siliciclastic rocks could have been retained in pores, or layer-parallel concentrations (calcareous layers?), and may have back-reacted during cooling to form carbonate cements and residual carbon species (pyrobitumen and graphite). (3) Carbon-rich gases and lower-temperature fluids from the distal thermal halo may have migrated into more depleted rocks located near the igneous contacts, refertilizing them. There are carbonate-bearing layers in the contact-proximal shale that may represent transient channels and carbonate-bearing veins (Figs. 3G and 3H), indicating the mobility of CO<sub>2</sub>-rich fluids. Neoblastic pyrites in the Hare Sill (Deegan et al., 2018) provide independent evidence that S-bearing gases/fluids percolated up from adjoining sedimentary rocks into the Hare Sill as it cooled. In conclusion, while it is clear that much of the Blaa Mountain Group was heated to >250 °C and has lost most of its original organic carbon, possibly to the atmosphere, the preservation of rocks high in organic carbon in our study area (Figs. 7 and 8) suggests that some of the thermogenic gas was trapped in situ, potentially mitigating the impact on paleoclimate.

### CONCLUSIONS

We document how Mesozoic High Arctic Large Igneous Province sills affected the fine-grained, organic-rich siliciclastic host rocks of the Sverdrup Basin in the Canadian Arctic Archipelago that they intruded. Petrographic and X-ray diffraction data reveal high-temperature metamorphic phases (diopside, andalusite, garnet, and cordierite) in the proximal aureoles. Raman thermometry on organic matter yields peak temperatures of 385–400 °C near sill contacts, tailing off to far-field temperatures of ~230–210 °C. Samples located >20 m from sills show no systematic change in vitrinite reflectance and have a VRo eq% value of ~2.5%, which translates to a temperature of ~210 °C. The finite element modeling tool SUTRAHEAT shows that contact-proximal rocks attain temperatures of >700 °C for ~1 year, but the temperature anomaly collapses rapidly after 5 years (full solidification). By 10 years, all rocks within 10 m of the Hare Sill are between 450 °C and 400 °C, rocks at 20 m from the contact attain 200 °C, yet far-field temperatures (>50 m) have barely changed. When multiple sills are emplaced, rocks halfway

between sills reach ~250 °C after 100 years. SILLi thermal modeling implies that much of the hydrocarbon-generating potential was eliminated by intrusion. The SILLi model suggests that ~20 tonnes/m<sup>2</sup> of organic equivalent-CO<sub>2</sub> gas was generated by the Hare sill alone, and ~226 tonnes/m<sup>2</sup> was generated by the multiple sill scenario. On a basin scale, this yields a total of ~2550 Gt CO<sub>2</sub> from single 17 m sill, with ~13,000 Gt CO<sub>2</sub> being generated by the multiple sill scenario, similar to estimates from other LIPs. Although it is predicted that most of the organic carbon in the Murray Harbour Formation rocks should have been converted to gas, our data from sill-proximal Murray Harbour rocks do not show complete removal of organic carbon, which suggests that not all of the carbon was expelled from the sedimentary package hosting High Arctic Large Igneous Province magmas. We speculate that a portion of the hydrocarbon gas and CO<sub>2</sub> generated by contact metamorphism back-reacted with the surrounding rocks due to the rarity of high-permeability conduits, and thus was not released into the atmosphere.

### ACKNOWLEDGMENTS

Fieldwork was funded by the Geological Survey of Canada, Polar Continental Shelf Project. Work by J.H. Bédard, S.E. Grasby, and K. Dewing was funded by the Geological Survey of Canada's GEM2 program. F.M. Deegan and V.R. Troll received financial support from the Swedish Research Council (grant nos. 2016-04838 and 2018-04933). The manuscript benefited by constructive and insightful comments from Ingrid Aarnes, Jennifer Galloway, and Nicolas Pinet. We thank the Polar Shelf pilots for their unflinching efficiency and good humor, and the staff of Resolute Base and Eureka Weather Station for their hospitality. This is Natural Resources Canada Geological Survey of Canada Contribution 20230095.

### REFERENCES CITED

- Aarnes, I., Svensen, H., Connolly, J.A.D., and Podladchikov, Y.Y., 2010, How contact metamorphism can trigger global climate changes: Modeling gas generation around igneous sills in sedimentary basins: *Geochimica et Cosmochimica Acta*, v. 74, p. 7179–7195, <https://doi.org/10.1016/j.gca.2010.09.011>.
- Aarnes, I., Svensen, H., Polteau, S., and Planke, S., 2011, Contact metamorphic devolatilization of shales in the Karoo Basin, South Africa, and the effects of multiple sill intrusions: *Chemical Geology*, v. 281, p. 181–194, <https://doi.org/10.1016/j.chemgeo.2010.12.007>.
- Ardakani, O., Sanei, H., Snowdon, L., Outridge, P.M., Obermajer, M., Stewart, R., Vandenberg, R., and Boyce, K., 2016, The accepted values for the internal Geological Survey of Canada (GSC) 9107 Rock-Eval 6@ standard (Upper Cretaceous Second White Speckled Shale, Colorado Group), western Canada: Geological Survey of Canada Open File 8043, <https://doi.org/10.4095/298729>.
- Baker, L.L., Bernard, A., Rember, W.C., Milazzo, M., Dundas, C., Abramov, O., and Keszthelyi, L., 2015, Temperature profile around a basaltic sill intruded into wet sediments: *Journal of Volcanology and Geothermal Research*, v. 302, p. 81–86, <https://doi.org/10.1016/j.jvolgeores.2015.06.012>.
- Bédard, J.H., Troll, V.R., and Deegan, F., 2016, HALIP intrusions, contact metamorphism, and incipient diapirism

- of gypsum-carbonate sequences, in Williamson, M.-C., ed., Report of activities for High Arctic Large Igneous Province (HALIP)—GEM 2 Western Arctic Region Project, Bedrock Mapping and Mineral Exploration: Geological Survey of Canada Open File 7950, p. 3–13.
- Bédard, J.H., Deegan, F.M., Troll, V.R., Dewing, K., Grasby, S.E., and Saumur, B.M., 2019, High Arctic Large Igneous Province magmatism in Canada: Geochemical and petrologic constraints on petrogenesis: Abstract presented 13–18 October 2019 at the American Geophysical Union, Chapman Conference, Large-Scale Volcanism in the Arctic: The Role of the Mantle and Tectonics, Selfoss, Iceland.
- Bédard, J.H., Saumur, B.M., Tegner, C., Troll, V.R., Deegan, F.M., Evenchick, C.A., Grasby, S.E., and Dewing, K., 2021a, Geochemical systematics of High Arctic Large Igneous Province continental tholeiites from Canada—Evidence for progressive crustal contamination in the plumbing system: *Journal of Petrology*, v. 62, no. 9, <https://doi.org/10.1093/petrology/egab041>.
- Bédard, J.H., Troll, V.R., Deegan, F., Tegner, C., Saumur, B.M., Evenchick, C., Grasby, S., and Dewing, K., 2021b, High Arctic Large Igneous Province alkaline rocks in Canada: Evidence for multiple mantle components: *Journal of Petrology*, v. 62, no. 9, <https://doi.org/10.1093/petrology/egab042>.
- Bond, D.P.G., and Grasby, S.E., 2017, On the causes of mass extinctions: Palaeogeography, Palaeoclimatology, Palaeoecology, v. 478, p. 3–29, <https://doi.org/10.1016/j.palaeo.2016.11.005>.
- Boudreau, A.E., 1999, PELE—A version of the MELTS software program for the PC platform: *Computers & Geosciences*, v. 25, p. 201–203, [https://doi.org/10.1016/S0098-3004\(98\)00117-4](https://doi.org/10.1016/S0098-3004(98)00117-4).
- Brooks, P.W., Embry, A.F., Goodarzi, F., and Stewart, R., 1992, Organic geochemistry and biological marker geochemistry of Schei Point Group (Triassic) and recovered oils from the Sverdrup Basin (Arctic Islands, Canada): *Bulletin of Canadian Petroleum Geology*, v. 40, p. 173–187.
- Buchan, K.L., and Ernst, R.E., 2006, Giant dyke swarms and the reconstruction of the Canadian Arctic Islands, Greenland, Svalbard and Franz Josef Land, in Hanski, E., Mertanen, S., Rämö, T., and Vuollo, J., eds., *Dyke Swarms: Time Markers of Crustal Evolution*: Taylor & Francis, p. 27–48.
- Bustin, R.M., 1986, Organic maturity of Late Cretaceous and Tertiary coal measures, Canadian Arctic Archipelago: *International Journal of Coal Geology*, v. 6, p. 71–106, [https://doi.org/10.1016/0166-5162\(86\)90026-1](https://doi.org/10.1016/0166-5162(86)90026-1).
- Daigle, H., Reece, J.S., and Flemings, P.B., 2019, Evolution of the percolation threshold in muds and mudrocks during burial: *Geophysical Research Letters*, v. 46, p. 8064–8073, <https://doi.org/10.1029/2019GL083723>.
- Deegan, F.M., Bédard, J.H., Troll, V.R., Whitehouse, M.J., Hagerfors, E., and Geiger, H., 2018, Sulphur mobilisation from sedimentary host rocks in the High Arctic Large Igneous Province: Abstract presented at the International Conference on Arctic Margins, VIII, Stockholm, 11–14 June.
- Deegan, F.M., Bédard, J.H., Grasby, S.E., Dewing, K., Geiger, H., Misiti, V., Capriolo, M., Callegaro, S., Svensen, H.H., Yakymchuk, C., Aradi, L.E., Freda, C., and Troll, V.R., 2022, Magma-shale interaction in Large Igneous Provinces, implications for climate warming and sulfide genesis: *Journal of Petrology*, v. 63, <https://doi.org/10.1093/petrology/egac094>.
- Dewing, K., and Embry, A.F., 2007, Geological and geochemical data from the Canadian Arctic Islands, Part I: Stratigraphic tops from Arctic Islands' oil and gas exploration boreholes: Geological Survey of Canada Open File Report 5442 (CD-ROM), <https://doi.org/10.4095/223386>.
- Dewing, K., and Obermajer, M., 2011, Chapter 38: Thermal maturity of the Sverdrup Basin, Arctic Canada and its bearing on hydrocarbon potential, in Spencer, M., Gautier, D., Stoupakova, A., Embry, A., and Sørensen K., eds., *Arctic Petroleum Geology*: Geological Society, London, Memoir 35, p. 567–580, <https://doi.org/10.1144/M35.38>.
- Dewing, K., and Sanei, H., 2009, Analysis of large thermal maturity data sets: Examples from the Canadian Arctic Islands: *International Journal of Coal Geology*, v. 77, p. 436–448, <https://doi.org/10.1016/j.coal.2008.04.009>.
- Dewing, K., Obermajer, M., and Goodarzi, F., 2007a, Geological and geochemical data from the Canadian Arctic Islands, Part III: Organic matter reflectance data: Geological Survey of Canada Open File 5476.
- Dewing, K., Obermajer, M., and Snowdon, L.R., 2007b, Geological and geochemical data from the Canadian Arctic Islands, Part VII: Composition of gas from petroleum exploration borehole cuttings: Geological Survey of Canada Open File 5611.
- Dockman, D.M., Pearson, D.G., Heaman, L.M., Gibson, S.A., and Sarkar, C., 2018, Timing and origin of magmatism in the Sverdrup Basin, Northern Canada—Implications for lithospheric evolution in the High Arctic Large Igneous Province (HALIP): *Tectonophysics*, v. 742–743, p. 50–65, <https://doi.org/10.1016/j.tecto.2018.05.010>.
- Døssing, A., Jackson, H.R., Matzka, J., Einarrsson, I., Rasmussen, T.M., Olesen, A.V., and Brozena, J.M., 2013, On the origin of the Amerasia Basin and the High Arctic Large Igneous Province: Results of new aeromagnetic data: *Earth and Planetary Science Letters*, v. 363, p. 219–230, <https://doi.org/10.1016/j.epsl.2012.12.013>.
- Dostal, J., and MacRae, A., 2018, Cretaceous basalts of the High Arctic large igneous province at Axel Heiberg Island (Canada): Volcanic stratigraphy, geodynamic setting, and origin: *Geological Journal*, v. 53, p. 2918–2934, <https://doi.org/10.1002/gj.3132>.
- Embry, A., and Beauchamp, B., 2019, Sverdrup Basin, in Miall, A.D., ed., *The Sedimentary Basins of the United States and Canada*: Elsevier, p. 559–592, <https://doi.org/10.1016/B978-0-444-63895-3.00014-0>.
- Embry, A.F., 1984, The Schei Point and Blaa Mountain Groups (Middle–Upper Triassic), Sverdrup Basin, Canadian Arctic Archipelago: Geological Survey of Canada Paper 84-1B, p. 327–336, <https://doi.org/10.4095/119589>.
- Embry, A.F., and Osadetz, K.G., 1988, Stratigraphy and tectonic significance of Cretaceous volcanism in the Queen Elizabeth Islands, Canadian Arctic Archipelago: *Canadian Journal of Earth Sciences*, v. 25, p. 1209–1219, <https://doi.org/10.1139/e88-118>.
- Ernst, R.E., 2014, Large Igneous Provinces: Cambridge University Press, <https://doi.org/10.1017/CBO9781139025300>.
- Estrada, S., 2015, Geochemical and Sr-Nd isotope variations within Cretaceous continental flood-basalt suites of the Canadian High Arctic, with a focus on the Hassel Formation basalts of northeast Ellesmere Island: *International Journal of Earth Sciences*, v. 104, p. 1981–2005, <https://doi.org/10.1007/s00531-014-1066-x>.
- Estrada, S., and Henjes-Kunst, F., 2004, Volcanism in the Canadian High Arctic Related to the Opening of the Arctic Ocean: *Journal of the German Society for Geosciences*, v. 154, no. 4, p. 579–603 [in German].
- Estrada, S., and Henjes-Kunst, F., 2013, <sup>40</sup>Ar–<sup>39</sup>Ar and U–Pb dating of Cretaceous continental rift-related magmatism on the northeast Canadian Arctic margin: *Journal of the German Society for Geosciences*, v. 164, no. 1, p. 107–130 [in German].
- Evenick, J.C., 2021, Examining the relationship between Tmax and vitrinite reflectance: An empirical comparison between thermal maturity indicators: *Journal of Natural Gas Science and Engineering*, v. 91, <https://doi.org/10.1016/j.jngse.2021.103946>.
- Frey, M., Capitani, C.D., and Liou, J.G., 1991, A new petrogenetic grid for low-grade metabasites: *Journal of Metamorphic Geology*, v. 9, p. 497–509, <https://doi.org/10.1111/j.1525-1314.1991.tb00542.x>.
- Frieling, J., Svensen, H.H., Planke, S., Chromwinckel, M.J., Selnes, H., and Sluijs, A., 2016, Thermogenic methane release as a cause for the long duration of the PETM: *Proceedings of the National Academy of Sciences of the United States of America*, v. 113, p. 12,059–12,064, <https://doi.org/10.1073/pnas.1603348113>.
- Galerne, C.Y., and Hasenclever, J., 2019, Distinct degassing pulses during magma invasion in the stratified Karoo Basin—New insights from hydrothermal fluid flow modeling: *Geochemistry, Geophysics, Geosystems*, v. 20, p. 2955–2984, <https://doi.org/10.1029/2018GC008120>.
- Galloway, J.M., Fensome, R.A., Swindles, G.T., Hadlari, T., Fath, J., Schröder-Adams, C., Herrle, J.O., and Pugh, A., 2022, Exploring the role of High Arctic Large Igneous Province volcanism on Early Cretaceous Arctic forests: *Cretaceous Research*, v. 129, <https://doi.org/10.1016/j.cretres.2021.105022>.
- Ganino, C., and Arndt, N.T., 2009, Climate changes caused by degassing of sediments during the emplacement of large igneous provinces: *Geology*, v. 37, p. 323–326, <https://doi.org/10.1130/G25325A.1>.
- Gentzis, T., Goodarzi, F., and Embry, A.F., 1996, Thermal maturation, potential source rocks and hydrocarbon generation in Mesozoic rocks, Lougheed Island area, Central Canadian Arctic Archipelago: *Marine and Petroleum Geology*, v. 13, p. 879–905, [https://doi.org/10.1016/S0264-8172\(96\)00028-1](https://doi.org/10.1016/S0264-8172(96)00028-1).
- Ghiorso, M.S., Hirschmann, M.M., Reiners, P.W., and Kress, V.C., III, 2002, The pMELTS: A revision of MELTS for improved calculation of phase relations and major element partitioning related to partial melting of the mantle: *Geochemistry, Geophysics, Geosystems*, v. 3, no. 5, <https://doi.org/10.1029/2001GC000217>.
- Goodarzi, F., Gentzis, T., and Dewing, K., 2019, Influence of igneous intrusions on the thermal maturity of organic matter in the Sverdrup Basin, Arctic Canada: *International Journal of Coal Petrology*, v. 213.
- Grasby, S.E., Beauchamp, B., and Knies, J., 2016, Early Triassic productivity crises delayed recovery from world's worst mass extinction: *Geology*, v. 44, p. 779–782, <https://doi.org/10.1130/G38141.1>.
- Guo, W., Zhang, X., Yu, R., Kang, L., Gao, L., and Liu, Y., 2022, A model for the apparent gas permeability of shale matrix organic nanopore considering multiple physical phenomena: *Frontiers of Earth Science*, v. 9, <https://doi.org/10.3389/feart.2021.813585>.
- Hayes, B., Bédard, J.H., and Lissenberg, C.J., 2015, Olivine slurry replenishment and the development of igneous layering in a Franklin Sill, Victoria Island, Arctic Canada: *Journal of Petrology*, v. 56, p. 83–112, <https://doi.org/10.1093/petrology/egu072>.
- Heimdal, T.H., Svensen, H.H., Ramezani, J., Iyer, K., Pereira, E., Rodrigues, R., and Callegaro, S., 2018, Large-scale sill emplacement in Brazil as a trigger for the end-Triassic crisis: *Scientific Reports*, v. 8, 141, p. 1–12, <https://doi.org/10.1038/s41598-017-18629-8>.
- Holland, T.J.B., and Powell, R., 2011, An improved and extended internally consistent thermodynamic dataset for phases of petrological interest, involving a new Equation of State for solids: *Journal of Metamorphic Geology*, v. 29, p. 333–383, <https://doi.org/10.1111/j.1525-1314.2010.00923.x>.
- Iyer, K., Svensen, H., and Schmid, D.W., 2018, SILLi 1.0: A 1-D numerical tool quantifying the thermal effects of sill intrusions: *Geoscientific Model Development*, v. 11, p. 43–60, <https://doi.org/10.5194/gmd-11-43-2018>.
- Jenkyns, H.C., Dickson, A.J., Ruhl, M., and Van den Boom, S.H., 2017, Basalt-seawater interaction, the Plenius Cold Event, enhanced weathering and geochemical change: Deconstructing Oceanic Anoxic Event 2 (Cenomanian–Turonian, Late Cretaceous): *Sedimentology*, v. 64, no. 1, p. 16–43, <https://doi.org/10.1111/sed.12305>.
- Jones, S.F., Wielens, H., Williamson, M.-C., and Zentilli, M., 2007, Impact of magmatism on petroleum systems in the Sverdrup basin, Canadian Arctic Islands, Nunavut: A numerical modelling study: *Journal of Petroleum Geology*, v. 30, p. 237–256, <https://doi.org/10.1111/j.1747-5457.2007.00237.x>.
- Kamber, B.S., Greig, A., and Collerson, K.D., 2005, A new estimate for the composition of weathered young upper continental crust from alluvial sediments, Queensland, Australia: *Geochimica et Cosmochimica Acta*, v. 69, p. 1041–1058, <https://doi.org/10.1016/j.gca.2004.08.020>.
- Kingsbury, C.G., Kamo, S.L., Ernst, R.E., Söderlund, U., and Cousens, B.L., 2018, U–Pb geochronology of the plumbing system associated with the Late Cretaceous Strand Fiord Formation, Axel Heiberg Island, Canada: Part of the 130–90 Ma High Arctic large igneous province: *Journal of Geodynamics*, v. 118, p. 106–117, <https://doi.org/10.1016/j.jog.2017.11.001>.
- Kondla, D., Sanei, H., Embry, A., Ardakani, O.H., and Clarkson, C.R., 2015, Depositional environment and hydrocarbon potential of the Middle Triassic strata of the Sverdrup Basin, Canada: *International Journal of Coal Geology*, v. 147–148, p. 71–84, <https://doi.org/10.1016/j.coal.2015.06.010>.

- Kouketsu, Y., Mizukami, T., Mori, H., Endo, S., Aoya, M., Hara, H., Nakamura, D., and Wallis, S., 2014, A new approach to develop the Raman carbonaceous material geothermometer for low-grade metamorphism using peak width: *The Island Arc*, v. 23, p. 33–50, <https://doi.org/10.1111/iar.12057>.
- Labus, M., and Labus, K., 2018, Thermal conductivity and diffusivity of fine-grained sedimentary rocks: *Journal of Thermal Analysis and Calorimetry*, v. 132, p. 1669–1676, <https://doi.org/10.1007/s10973-018-7090-5>.
- Lafargue, E., Marquis, F., and Pillot, D., 1998, Rock-Eval 6 applications in hydrocarbon exploration, production, and in soil contamination studies: *Revue de l'Institut Français du Pétrole*, v. 53, p. 421–437, <https://doi.org/10.2516/ogst:1998036>.
- Landis, C.R., and Castaño, J.R., 1995, Maturation and bulk chemical properties of a suite of solid hydrocarbons: *Organic Geochemistry*, v. 22, p. 137–149, [https://doi.org/10.1016/0146-6380\(95\)90013-6](https://doi.org/10.1016/0146-6380(95)90013-6).
- Latypov, R.M., 2003, The origin of basic-ultrabasic sills with S-, D-, and I-shaped compositional profiles by in situ crystallization of a single input of phenocryst-poor parental magma: *Journal of Petrology*, v. 44, p. 1619–1656, <https://doi.org/10.1093/petrology/egg051>.
- Leclerc, F., Bédard, J.H., Harris, L.B., McNicoll, V.J., Goulet, N., Roy, P., and Houle, P., 2011, Tholeiitic to calc-alkaline cyclic volcanism in the Roy Group, Chibougamau area, Abitibi Greenstone Belt—Revised stratigraphy and implications for VHMS exploration: *Canadian Journal of Earth Sciences*, v. 48, no. 3, p. 661–694, <https://doi.org/10.1139/E10-088>.
- Liou, J.G., 1971, Synthesis and stability relations of prehnite,  $\text{Ca}_2\text{Al}_2\text{Si}_2\text{O}_{10}(\text{OH})_2$ : *The American Mineralogist*, v. 56, p. 507–531.
- Maher, H.D.J., 2001, Manifestations of the Cretaceous High Arctic Large Igneous Province in Svalbard: *The Journal of Geology*, v. 109, p. 91–104, <https://doi.org/10.1086/317960>.
- Mastalerz, M., Drobnik, A., and Stankiewicz, A.B., 2018, Origin, properties, and implications of solid bitumen in source-rock reservoirs: *International Journal of Coal Geology*, v. 195, p. 14–36, <https://doi.org/10.1016/j.coal.2018.05.013>.
- Mukhopadhyay, P.K., Goodarzi, F., Kruger, M.A., and Alimi, M.H., 1997, Comparison of source rock geochemistry of selected rocks from the Schei Point Group and Ringnes Formation, Sverdrup Basin, Arctic Canada: *International Journal of Coal Geology*, v. 34, p. 225–260, [https://doi.org/10.1016/S0166-5162\(97\)00024-4](https://doi.org/10.1016/S0166-5162(97)00024-4).
- Nabelek, P., and Chen, Y., 2019, SUTRAHEAT: A program for modeling conductive heat transport in and around growing magma chambers: *Zenodo*, <https://doi.org/10.5281/zenodo.3537680>.
- Nabelek, P.I., Hofmeister, A.M., and Whittington, A.G., 2012, The influence of temperature-dependent thermal diffusivity on the conductive cooling rates of plutons and temperature-time paths in contact aureoles: *Earth and Planetary Science Letters*, v. 317–318, p. 157–164, <https://doi.org/10.1016/j.epsl.2011.11.009>.
- Nabelek, P.I., Bédard, J.H., and Rainbird, R.H., 2014, Numerical constraints on degassing of metamorphic  $\text{CO}_2$  during the Neoproterozoic Franklin large igneous event, Arctic Canada: *Geological Society of America Bulletin*, v. 126, p. 759–772, <https://doi.org/10.1130/B30981.1>.
- Naber, T.V., Grashby, S.E., Cuthbertson, J.P., Rayner, N., and Tegner, C., 2021, Tracing the extension of the Alpha Ridge onto Ellesmere Island, Canada: New constraints on the age and geochemistry of High Arctic Large Igneous Province magmatism: *Geological Society of America Bulletin*, v. 133, p. 1695–1711, <https://doi.org/10.1130/B35792.1>.
- Nielsen, S.B., Clausen, O.R., and McGregor, E., 2017, basin%Ro: A vitrinite reflectance model derived from basin and laboratory data: *Basin Research*, v. 29, p. 515–536, <https://doi.org/10.1111/bre.12160>.
- Obermajer, M., Stewart, K.R., and Dewing, K., 2007, Geological and geochemical data from the Canadian Arctic Islands, Part II: Rock-Eval/TOC data: *Geological Survey of Canada Open File 5459*, CD-ROM, <https://doi.org/10.4095/223457>.
- Planke, S., Polteau, S., Senger, K., Svendsen, H.H., Faleide, J.I., Myklebust, R., and Tegner, C., 2017, HALIP intrusive and extrusive complexes of Svalbard and the Barents Sea, *in* Williamson, M.C., ed., *GEM 2 High Arctic Large Igneous Province (HALIP) Activity: Workshop Report: Geological Survey of Canada Open File 8151*, p. 4–6, <https://doi.org/10.4095/300700>.
- Ruhl, M., and Kürschner, W.M., 2011, Multiple phases of carbon cycle disturbance from large igneous province formation at the Triassic–Jurassic transition: *Geology*, v. 39, p. 431–434, <https://doi.org/10.1130/G31680.1>.
- Sanei, H., Wood, J.M., Ardakani, O.H., Clarkson, C.R., and Jiang, C., 2015, Characterization of organic matter fractions in an unconventional tight gas siltstone reservoir: *International Journal of Coal Geology*, v. 150–151, p. 296–305, <https://doi.org/10.1016/j.coal.2015.04.004>.
- Saumur, B.M., Dewing, K., and Williamson, M.-C., 2016, Architecture of the Canadian portion of the High Arctic Large Igneous Province and implications for magmatic Ni-Cu potential: *Canadian Journal of Earth Sciences*, v. 53, p. 528–542, <https://doi.org/10.1139/cjes-2015-0220>.
- Saumur, B.M., Bédard, J.H., and Williamson, M.-C., 2022, Targeting magmatic Ni-Cu mineralization within large igneous provinces: An integrated approach for the High Arctic LIP: *Mineralium Deposita*, v. 57, p. 207–233, <https://doi.org/10.1007/s00126-021-01054-3>.
- Savard, D., Barnes, S.-J., and Meisel, T., 2010, Comparison between nickel-sulfur fire assay Te Co-Precipitation and isotope dilution with high-pressure asher acid digestion for the determination of platinum-group elements, rhenium and gold: *Geostandards and Geoanalytical Research*, v. 34, <https://doi.org/10.1111/j.1751-908X.2010.00900.9x>.
- Schröder-Adams, C.J., Herrle, J.O., Selby, D., Quesnel, A., and Froude, G., 2019, Influence of the high Arctic igneous province on the Cenomanian/Turonian boundary interval, Sverdrup Basin, High Canadian Arctic: *Earth and Planetary Science Letters*, v. 511, p. 76–88, <https://doi.org/10.1016/j.epsl.2019.01.023>.
- Self, S., Schmidt, A., and Mather, T.A., 2014, Emplacement characteristics, time scales, and volcanic gas release rates of continental flood basalt eruptions on Earth, *in* Keller, G., and Kerr, A.C., eds., *Volcanism, Impacts, and Mass Extinctions: Causes and Effects: Geological Society of America Special Paper 505*, p. 319–337, [https://doi.org/10.1130/2014.2505\(16\)](https://doi.org/10.1130/2014.2505(16)).
- Skippen, G., 1974, An experimental model for low pressure metamorphism of siliceous dolomitic marble: *American Journal of Science*, v. 274, p. 487–509, <https://doi.org/10.2475/ajs.274.5.487>.
- Spacapan, J.B., Palma, J.O., Galland, O., Manceda, R., Rocha, E., D'Odorico, A., and Leanza, H.A., 2018, Thermal impact of igneous sill-complexes on organic-rich formations and implications for petroleum systems: A case study in the northern Neuquén Basin, Argentina: *Marine and Petroleum Geology*, v. 91, p. 519–531, <https://doi.org/10.1016/j.marpetgeo.2018.01.018>.
- Spear, F.S., and Cheney, J.T., 1989, A petrogenetic grid for pelitic schists in the system  $\text{SiO}_2\text{-Al}_2\text{O}_3\text{-FeO-MgO-K}_2\text{O-H}_2\text{O}$ : *Contributions to Mineralogy and Petrology*, v. 101, p. 149–164, <https://doi.org/10.1007/BF00375302>.
- Stolper, D.A., Lawson, M., Davis, C.L., Ferreira, A.A., Santos Neto, E.V., Ellis, G.S., Lewan, M.D., Martini, A.M., Tang, Y., Schoell, M., Sessions, A.L., and Eiler, J.M., 2014, Formation temperatures of thermogenic and biogenic methane: *Science*, v. 344, p. 1500–1503, <https://doi.org/10.1126/science.1254509>.
- Svendsen, H.H., Planke, S., Malthe-Sørensen, A., Jamtveit, B., Myklebust, R., Eidem, T.R., and Rey, S.S., 2004, Release of methane from a volcanic basin as a mechanism for initial Eocene global warming: *Nature*, v. 429, p. 542–545, <https://doi.org/10.1038/nature02566>.
- Svendsen, H.H., Planke, S., Chevallier, L., Malthe-Sørensen, A., Corfu, F., and Jamtveit, B., 2007, Hydrothermal venting of greenhouse gases triggering Early Jurassic global warming: *Earth and Planetary Science Letters*, v. 256, p. 554–566, <https://doi.org/10.1016/j.epsl.2007.02.013>.
- Svendsen, H.H., Planke, S., Polozov, A.G., Schmidtbauer, N., Corfu, F., Podladchikov, Y.Y., and Jamtveit, B., 2009, Siberian gas venting and the end-Permian environmental crisis: *Earth and Planetary Science Letters*, v. 277, p. 490–500, <https://doi.org/10.1016/j.epsl.2008.11.015>.
- Svendsen, H.H., Frolov, S., Akhmanov, G.G., Polozov, A.G., Jerram, D.A., Shiganova, O.V., Melnikov, N.V., Iyer, K., and Planke, S., 2018, Sills and gas generation in the Siberian Traps: *Philosophical Transactions of the Royal Society A: Mathematical, Physical and Engineering Sciences*, v. 376, <https://doi.org/10.1098/rsta.2017.0080>.
- Svendsen, H.H., Hammer, Ø., Chevallier, L., Jerram, D.A., Silkose, P., Polteau, S., and Planke, S., 2020, Understanding thermogenic degassing in large igneous provinces: Inferences from the geological and statistical characteristics of breccia pipes in the western parts of the Karoo Basin, *in* Adatte, T., Bond, D.P.G., and Keller, G., eds., *Mass Extinctions, Volcanism, and Impacts: New Developments: Geological Society of America Special Paper 544*, p. 67–84, [https://doi.org/10.1130/2020.2544\(03\)](https://doi.org/10.1130/2020.2544(03)).
- Sweeney, J.J., and Burnham, A.K., 1990, Evaluation of a simple model of vitrinite reflectance based on chemical kinetics: *American Association of Petroleum Geologists Bulletin*, v. 74, p. 1559–1570.
- Sydes, M., Fjeldskaar, W., Fjeldskaar Løvteit, I., and Grunnaleite, I., 2018, The importance of sill thickness and timing of sill emplacement on hydrocarbon maturation: *Marine and Petroleum Geology*, v. 89, p. 500–514, <https://doi.org/10.1016/j.marpetgeo.2017.10.017>.
- Tegner, C., Storey, M., Holm, P.M., Thorarinsson, S.B., Zhao, X., Lo, C.H., and Knudsen, M.F., 2011, Magmatism and Eureka deformation in the High Arctic Large Igneous Province:  $^{40}\text{Ar}$ – $^{39}\text{Ar}$  age of Kap Washington Group Volcanics, North Greenland: *Earth and Planetary Science Letters*, v. 303, p. 203–214, <https://doi.org/10.1016/j.epsl.2010.12.047>.
- Tozer, E.T., 1961, Triassic Stratigraphy and Faunas, Queen Elizabeth Islands, Arctic Archipelago: *Geological Survey of Canada Memoir 316*, 184 p., <https://doi.org/10.4095/100543>.
- Uchikawa, J., Harper, D.T., Penman, D.E., Zachos, J.C., and Zeebe, R.E., 2017, Influence of solution chemistry on the boron content in inorganic calcite grown in artificial seawater: *Geochimica et Cosmochimica Acta*, v. 218, p. 291–307, <https://doi.org/10.1016/j.gca.2017.09.016>.
- Velde, B., 1978, High temperature or metamorphic vermiculites: *Contributions to Mineralogy and Petrology*, v. 66, p. 319–323, <https://doi.org/10.1007/BF00373416>.
- Voss, C.I., and Provost, A.M., 2002, A model for saturated-unsaturated, variable-density ground-water flow with solute or energy transport: *U.S. Geological Survey Water Resources Investigations Report WRI-02-4231*.
- Wang, D., and Manga, M., 2015, Organic matter maturation in the contact aureole of an igneous sill as a tracer of hydrothermal convection: *Journal of Geophysical Research: Solid Earth*, v. 120, p. 4102–4112, <https://doi.org/10.1002/2015JB011877>.
- Wang, K., Li, X., Chen, M., Ma, Y., Liu, K., Liu, L., Li, X., and Hu, W., 2012, Numerical modeling of the hydrocarbon generation of Tertiary source rocks intruded by doleritic sills in the Zhanhua depression, Bohai Bay Basin, China: *Basin Research*, v. 24, p. 234–247, <https://doi.org/10.1111/j.1365-2117.2011.00518.x>.
- Wang, M., Lu, S., Xue, H.T., Wu, J., and Liu, D.W., 2010, The effects of magmatic intrusions on the maturation of organic matter and its numerical simulation: *Acta Petrologica Sinica*, v. 26, p. 177–184.
- Williamson, M.-C., Saumur, B.-M., and Evenchick, C., 2016, HALIP volcanic-intrusive complexes, Axel Heiberg Island, Nunavut, *in* Williamson, M.-C., ed., *Report of Activities for High Arctic Large Igneous Province (HALIP)—GEM 2 Western Arctic Region Project: Bedrock Mapping and Mineral Exploration: Geological Survey of Canada Open File 7950*, p. 14–26.
- Zhang, K., Jiang, Z., Xie, X., Gao, Z., Liu, T., Yin, L., Jia, C., Song, Y., Shan, C., Wu, Y., and Wang, P., 2018, Lateral Percolation and Its Effect on Shale Gas Accumulation on the Basis of Complex Tectonic Background: *Hindawi Geofluids*, v. 2018, <https://doi.org/10.1155/2018/5195469>.

SCIENCE EDITOR: MIHAI DUCEA

MANUSCRIPT RECEIVED 24 FEBRUARY 2023  
 REVISED MANUSCRIPT RECEIVED 6 JUNE 2023  
 MANUSCRIPT ACCEPTED 18 JULY 2023

Printed in the USA